SANDIA REPORT

SAND2001-1441
Unlimited Release
Printed May 2001

Analysis of a Composite Blade Design for the AOC 15/50 Wind Turbine Using a Finite Element Model

Ladean R. McKittrick, Douglas S. Cairns, John Mandell, David C. Combs,
Donald A. Rabern, and R. Daniel Van Luchene

Prepared by
Sandia National Laboratories
Albuquerque, New Mexico 87185 and Livermore, California 94550

Sandia is a multiprogram laboratory operated by Sandia Corporation,
a Lockheed Martin Company, for the United States Department of Energy under Contract DE-AC04-94AL85000.

Sandia National Laboratories

Issued by Sandia National Laboratories, operated for the United States Department of Energy by Sandia Corporation.

Available to DOE and DOE contractors from
U.S. Department of Energy
Office of Scientific and Technical Information
P.O. Box 62
Oak Ridge, TN 37831

Telephone: (865)576-8401
Facsimile: (865)576-5728
E-Mail: reports@adonis.osti.gov
Online ordering: http://www.doe.gov/bridge

Available to the public from
U.S. Department of Commerce
National Technical Information Service
5285 Port Royal Rd
Springfield, VA 22161

Telephone: (800)553-6847
Facsimile: (703)605-6900
E-Mail: orders@ntis.fedworld.gov
Online order: http://www.ntis.gov/ordering.htm

SAND2001-1441
Unlimited Release
Printed May 2001

Analysis of a Composite Blade Design for the AOC 15/50 Wind Turbine Using a Finite Element Model

Ladean R. McKittrick, Douglas S. Cairns, P.I., John Mandell,
David C. Combs, Donald A. Rabern, and R. Daniel VanLuchene
College of Engineering
Montana State University
Bozeman, MT 59717

Abstract

A fiberglass blade was designed for the Atlantic Orient Corporation (AOC) 15/50 wind turbine through the use of finite element (FE) modeling techniques. In this initial design phase, the goals were: 1) make the blade as stiff as the previously designed laminated wood blade, 2) minimize resonant operating conditions, 3) design the blade to withstand extreme wind conditions, and 4) make the blade compatible with reasonable manufacturing techniques. The modeling assumptions used are discussed and the final results, for this initial design phase, are presented. Based on the FE model, the designed blade will be able to withstand extreme wind conditions through elastic deformation, and resonant operating conditions will be minimized.

This document is an overview of the design and manufacturing synthesis data of composite wind turbine blades for applications to the Sandia National Laboratories' NuMAD wind turbine blade design tool.

Acknowledgments

The authors give special thanks to Tom Ashwill, Herb Sutherland, Daniel Laird, and Henry Dodd of Sandia National Laboratories for their guidance and support for this effort. Thanks are also due to Bruce Johnson and Bob Sherwin of the Atlantic Orient Corporation for providing design specifications and field data from the AOC 15/50 wind turbine.

The basic blade design was completed under Montana DOE EPSCoR, Wind Energy Cluster Contract #DE-F02-91-ER-75681. This document was prepared as partial fulfillment of Sandia contract BC-3536.

Contents

List of Figures

List of Tables

Unit Conversions

	English	Metric
Length	1 inch	2.540 cm
	1 foot	0.305 m
	1 yard	0.914 m
Area	1 inch^2	6.452 cm^2
	1 foot^2	0.0930 m^2
Mass	1 lbm	0.454 kg
Force	1 lbf	4.448 N
	1 kip	4.448 kN
Pressure (Stress)	1 psi	6.895 kPa
	1 ksi	6.895 MPa
Velocity	1 MPH	0.447 m s^{-1}

Executive Summary

A glass-reinforced polyester (GRP) blade was designed for the AOC 15/50 wind turbine via finite element (FE) analysis techniques, following a previous design for a stiff laminated-wood epoxy (LWE) blade.

The final design, presented in this report, was reached through an iterative analysis process. First GRP layups were modified to obtain an approximate stiffness match with the LWE blade in the flapwise direction. Very little attention was given to matching edgewise stiffness. The flapwise stiffness match was the first and biggest step requiring several iterations. The layup was then modified in order to minimize the probability of harmonic excitations due to periodic variations in applied loads. The layup was additionally modified to endure extreme wind loads with buckling responses and maximum strains used as criteria for modifications. Final modifications were made in order to optimize torsional stiffness of the blade, in order to maintain an efficient angle of attack under operational loads.

For the final design, the FE model indicated that the natural frequencies of the composite blade were all above 3.5 Hz but were likely to vary significantly as a function of the mass associated with the tip brake structure. When compared with a rotational frequency on the order of 1 Hz and a first tower frequency of 1.7 Hz, the primary concern was the possibility of a mode interaction between the tower and the blade if the mass associated with the tip brake was sufficient to drive the blade frequency down to approximately 3.4 Hz (twice the fundamental frequency of the tower), making blade-tower resonance a possibility.

Extreme wind loads were also considered as part of the blade design, with a design wind speed of 133 MPH (i.e., with the wind turbine in a shutdown mode). For such a load case, the FE model indicated that peak strains would occur where the blade layup transitions from the heavy root layup to a thinner outboard layup. In the span-wise (primary-fiber) direction, peak strains were approximately 0.45% (~70% of ultimate); in the circumferential (transverse-fiber) direction, peak strains were approximately 0.27% (~55% of ultimate). The FE model, with non-linear geometry effects included, indicated that buckling was not likely to occur until the statically-equivalent distributed-load of 4200 lb (associated with a 133 MPH wind condition) was exceeded by more than 70%.

Yaw effects due to extreme wind shear were also considered. In one case, inertial loads were applied to represent a yaw velocity of 45 deg s^{-1}; in a second case, inertial loads were applied to represent a yaw acceleration of 470 deg s^{-2}. Both of these cases yielded lower strains than those resulting from the statically equivalent wind speed load of 4200 lb.

In summary, based on the FE analyses, the blade design is not overly conservative but the model indicates that it should be able to withstand extreme wind conditions. The model also indicates that deflections due to resonant conditions should be minimal.

1 Introduction

This report is a summary of the finite element modeling techniques and corresponding results that were used in the initial phase of the design of a wind turbine blade. The objective of this design process was the development of a blade design, using composite (fiberglass) materials and manufacturing techniques that could be used to replace the laminated wood epoxy blade presently used with the AOC 15/50 wind turbine. A second objective was the development of a general strategy that could be used in the design of wind turbine blades. This report represents the initial stage in the obtainment of both of these objectives.

The wood blade for the AOC 15/50 was originally designed by the Atlantic Orient Corporation[1] (AOC) in conjunction with MDZ Consulting[2] and was constructed by Guegon Bros. Inc.[3] using a laminated wood epoxy (LWE) layup. The blade's shape is taken from the NREL thick series (Tangler and Somers, 1995), which provides sufficient stiffness for tip brake attachments. The three-bladed rotor has a diameter of 15 m and is attached to the hub atop a tower that is typically 24 m tall. The overall geometry of the wind turbine is displayed in Figure 1.

The blade design presented here uses the same airfoil family and follows the same design criteria as those used for the wood blade. The primary goals in this initial design of the glass reinforced polyester (GRP) replacement-blade were:

- follow a "stiff-blade" design as was used for the laminated wood blade,
- minimize resonant conditions that can induce large damaging deflections,
- design the blade to withstand extreme wind events,
- optimize details for performance and manufacturing.

With the "stiff-blade" design philosophy, the blade is designed to withstand extreme loads through elastic deformation, rather than by inertial displacements as with a "soft-blade" design. For a stiff-blade design, the natural frequencies of the blade must be well above the one per-revolution frequency of the turbine rotor ($\sim$1.1 Hz). At the same time, the blade frequencies must be such that they will not interact with the fundamental vibrations of the tower, lowest of which, for the typical AOC 15/50 wind turbine lattice-tower, occurs at a frequency of $\sim$1.7 Hz.

Extreme winds can induce large strains through direct pressure and/or yawing effects of the turbine about the tower axis due to uneven wind loads. Both load cases were considered and are discussed in this report.

---

[1] AOC, P.O. Box 1097, Norwich, VT 05055 USA

[2] Mike Zuteck, 931 Grove, Kemah, TX 77565 USA

[3] Guegon Bros. Inc, Pinconning, MI 48650 USA

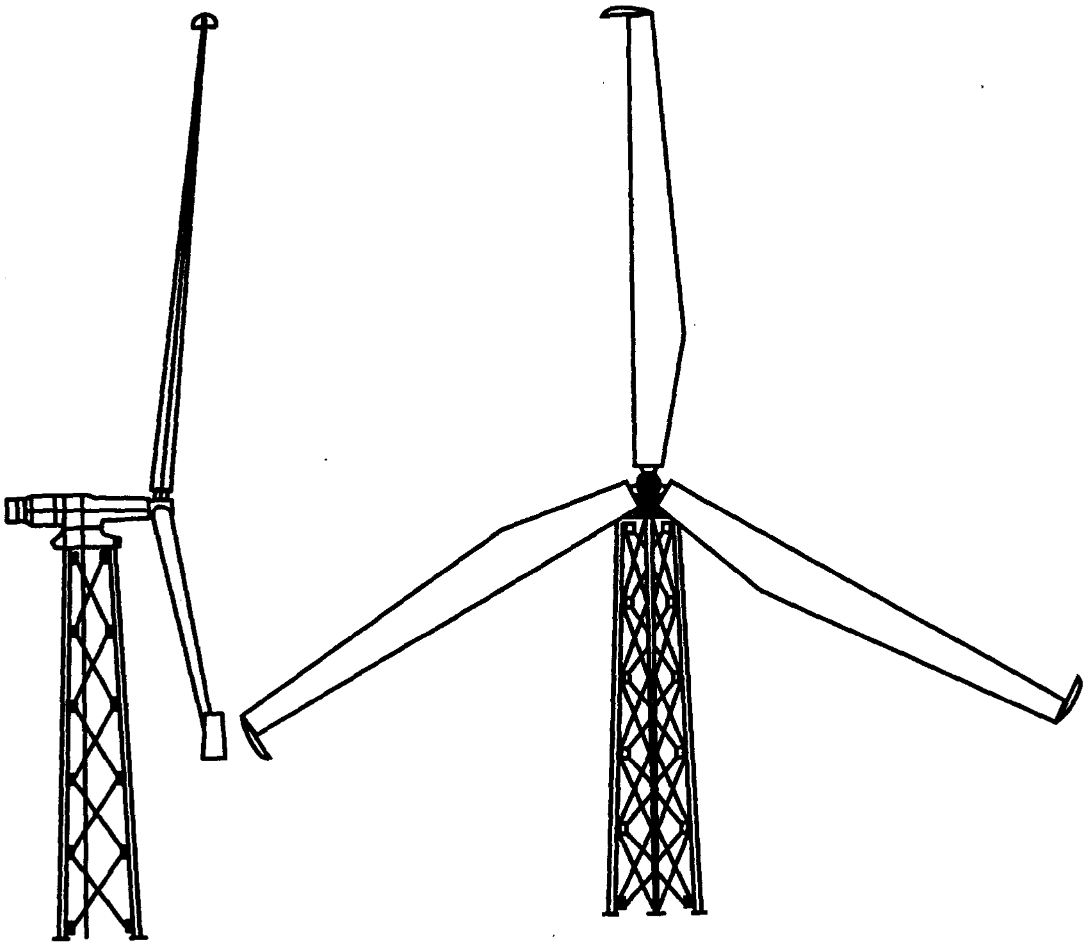

Figure 1: Top section of the tower and AOC 15/50 Wind Turbine.

2 FE Model

2.1 Blade Geometry

At each station along the length of the blade, the airfoil shape is the same as that for the AOC 15/50 wood blade, which has a length of 7.5 m (~295 in). The root of the blade starts at the hub connection, at a radius 11 inches from the center of the hub. At the root end of the blade, the cross-sectional shape is relatively oval and is only semi-aerodynamic. From the root region, the blade transitions from an oval shape to an aerodynamic shape at 40% of the tip radius as defined by the SERI 821 airfoil classification. Outboard from the root region, the shape transition continues spanwise to a shape is based on a SERI 819 airfoil at 75% of the tip radius and a shape that is based on a SERI 820 airfoil at 95% of the tip radius. These shapes and their aerodynamic characteristics are discussed in Tangler and Somers (1985, 1986); NREL (1994); Lissaman (1994); Tangler and Somers (1995).

Individual cross sections were defined using a "connect-the-dots" approach, i.e., cross-sections were defined with sets of 902 points (not nodes) that were distributed around the circumference of the blade. There were 20 of these point sets that were stationed along the span of the blade. In the circumferential direction, the skin of the blade was divided into fourteen increments. Each of these increments was modeled with a spline that passed through a subset of the points in each of the 20 point sets. Similarly, span-wise variations were modeled with splines that passed through skin cross section points at each of the 20 stations that spanned the length of the blade.

These splines, displayed in Figure 2, were defined so that they corresponded to changes in the material layup. Circumferential splines 1 and 2 defined the trailing edge for the high-pressure (bottom) surface of the trailing edge, while splines 13 and 14 defined the low pressure (top) surface of the trailing edge. Splines 4 and 5 defined the lower spar cap while splines 10 and 11 defined the upper spar cap. Splines 7 and 8, respectively, defined the high and low pressure faces of the leading edge. Splines 3, 6, 9, and 12 were used to define transitions between the spar cap and the leading and trailing edges. In this model, the spar began 32 inches outboard from the root end of the blade (at $z = 43$ in) and ended 17 inches inboard from the tip of the blade (at $z = 278$ in). Spanwise, the spar cap extended the full length of the blade; chordwise, the spar cap extended 3.5 inches from the center of the spar in each direction and transitioned into the leading and trailing edges over a distance of 0.65 inches.

Once the splines were defined, the span-wise surfaces were divided into six span-wise sectional areas that generally corresponded to AOC layup transitions in the original laminated wood blade. All skin areas (displayed in Figure 2) were generated in this manner.

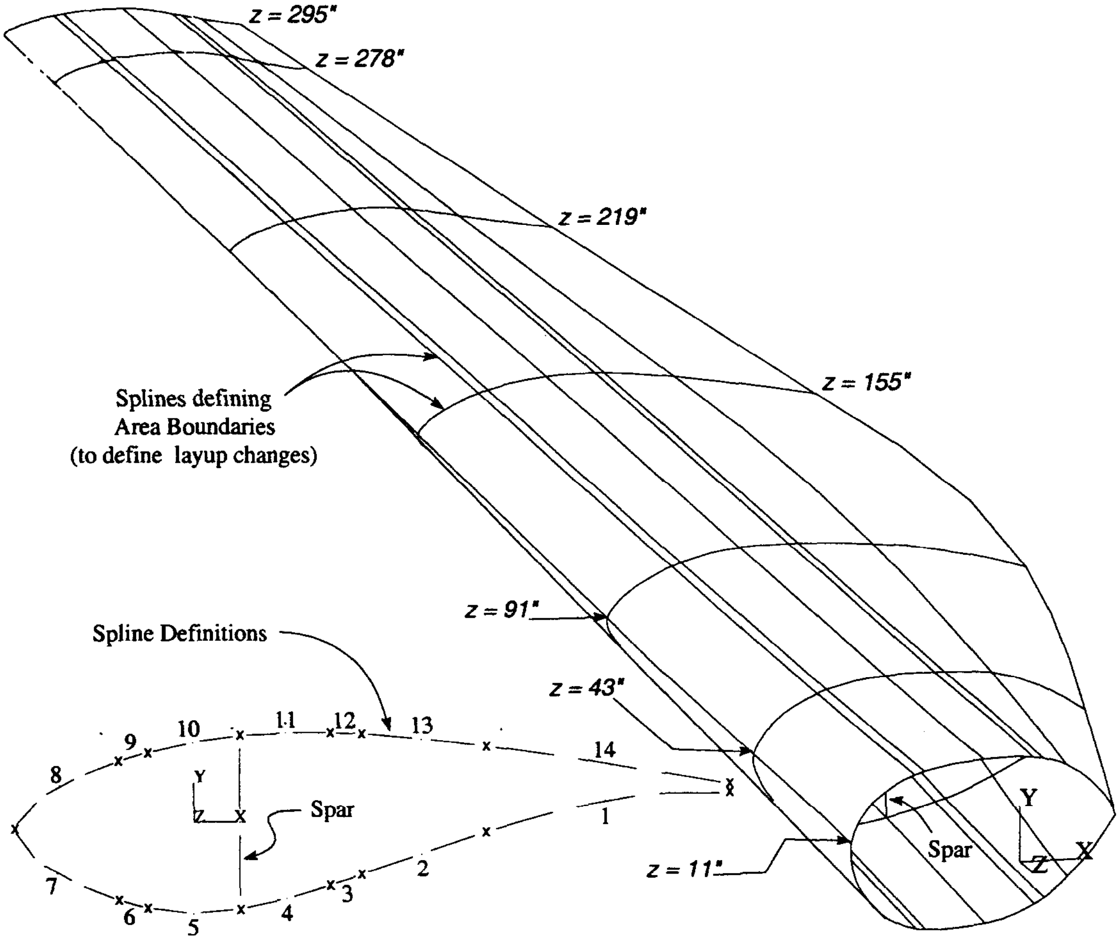

Figure 2: Spline used to define airfoil (blade) geometry. Numbers 1 through 14 refer to the individual splines while x's denote spline endpoints.

2.2 Blade Layup

For the finite element model (FEM), developed using ANSYS (V54), the structure of the blade was modeled with shell elements (ANSYS element types SHELL91 and SHELL99) capable of representing layer characteristics throughout the shell thickness. The boundaries between regional areas, displayed in Figure 2, were used to define major transitions due to ply drops. Most transitions due to ply drops were modeled as linear variations that occurred over the width of an element at the boundary between two layup regions. Regions of "constant" layup thickness were modeled according to the layup schedule presented in Figure 3b. Layup boundaries are displayed in Figure 2.

For the overall design and analysis of the blade, the ply layup in the root region (11 to 43 in) was considered "stiff" relative to the outboard sections of the blade. As a consequence, the root

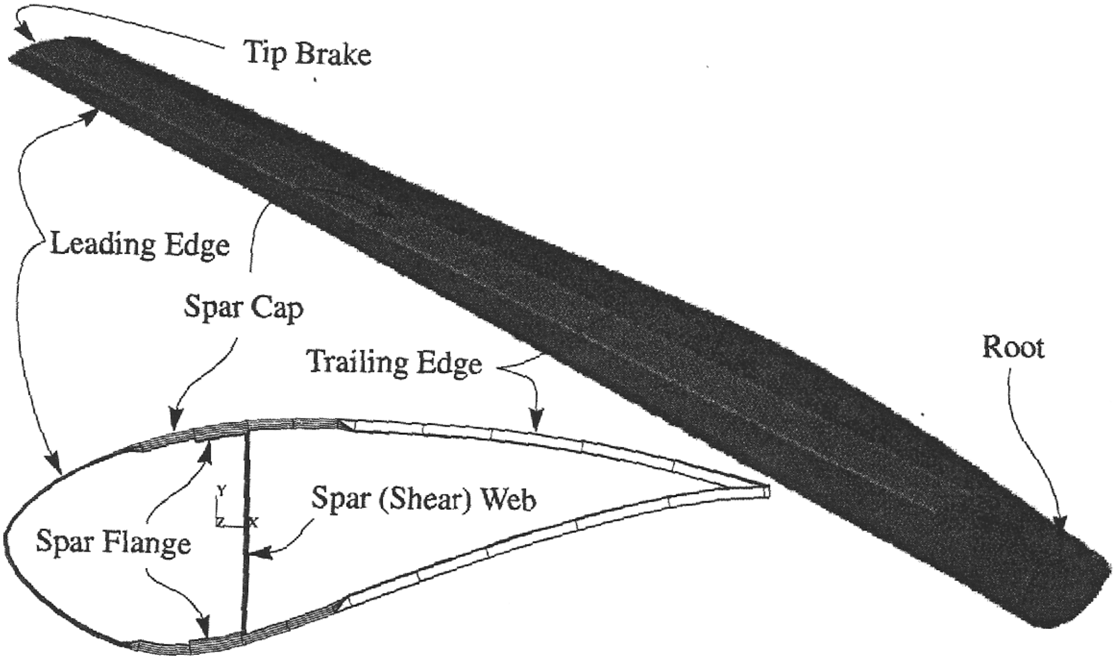

(a) graphic display of components in layup schedule

Component	Radius (%)	Z Location (inches)	Layup Schedule	Thickness (inches)
Root	3.7 to 10	11 to 30.5	$[\pm45/0_6/\pm45/0_6/+45]_s$	0.620
	10 to 12	30.5 to 35	$[\pm45/0_5/\pm45/0_5/+45]_s$	0.530
	12 to 15	35 to 43	$[\pm45/0_4/\pm45/0_4/+45]_s$	0.440
Spar Cap	15 to 31	43 to 91	$[\pm45/0_4/\pm45/0_4/+45]_s$	0.440
	31 to 53	91 to 155	$[\pm45/0_3/\pm45/0_3/+45]_s$	0.350
	53 to 74	155 to 219	$[\pm45/0_2/\pm45/0_2/+45]_s$	0.260
	74 to 100	219 to 295	$[\pm45/0/\pm45/0/+45]_s$	0.170
Leading Edge	15 to 31	43 to 91	$[\pm45/0_2/\pm45]_s$	0.154
	31 to 100	91 to 295	$[\pm45/0/\pm45]_s$	0.109
Trailing Edge	15 to 85	43 to 260	[±45/0/balsa/0/±45]	0.452
	85 to 100	260 to 295	$[\pm45/0]_s$	0.077
Spar (Shear) web	15 to 94	43 to 278	$[\pm45/0_2/\pm45]_s$	0.158
Spar Flange	15 to 100	43 to 295	$[\pm45/0_2/\pm45]_s$	0.154

(b) layup schedule

Figure 3: Layup schedule for composite AOC 15/50 blade.

layup was not modeled in detail but was instead modeled with a constant thickness of 0.62". In the next stage of the design process, the design of the root connection will be the primary focus. In this next phase, the layup in the root region will be modeled in more detail.

2.3 Material Parameters

Each of the GRP layers in the layup is modeled as orthotropic in a given layer, with two of the principal material axes in the plane of the shell. The orientation of the material axes (fiber directions) varies from one layer to the next. Material parameters listed in Table 1 were used to model various layers in the GRP layup.

The parameters listed in Table 1 were derived from experimental data (Mandell and Samborsky, 1997). The A130, D155 and DB120 lamina use E-glass fibers that are embedded in polymer matrix. Both the A130 and D155 lamina were considered for the 0 degree ply layups, but, because D155 lamina could not be obtained with continuous fibers greater than four feet in length, the properties for the A130 layup were the only ones used in the present study for 0 degree layups. The DB120 lamina was used for the ± 45 degree ply layups. Balsa wood was used as a filler in sandwich-type layups to minimize the probability of buckling while minimizing increased weight.

2.4 Ultimate Strains

The failure criteria used for designing the GRP blade were relatively simple. Stresses vary widely from layer to layer due to the changes in moduli and fiber orientation. Strains on the other hand, to meet compatibility, must be relatively consistent from layer to layer. This is particularly true for those portions of the blade skin that are positioned relatively far from the neutral axis of the blade. As a consequence, failure criteria were based entirely on strains. Ultimate (allowable) strains were based on the experimental values reported in Mandell and Samborsky (1997, Tab.9a). The strains of interest are listed in Table 2.

2.5 Boundary Conditions

At the root end of the blade, the connection to the hub was assumed to be rigid, relative to the blade. As a consequence, all six degrees of freedom for the nodes in the root plane of the blade (11 inches from the hub center) were fixed. Beyond this constraint, no other displacement constraints were imposed on the blade model.

		Layup Material				
		A130 (0's)	D155 (0's)	DB120 (±45's)	Balsa	Aluminum
$E_L = E_x$	GPa	31.7	38.3	26.2	0.187	24.1
	Msi	4.6	5.56	3.8	0.0271	3.5
$E_T = E_y$	GPa	7.58	6.89	6.55	0.061	24.1
	Msi	1.1	1.0	0.95	0.00885	3.5
$E_Z = E_z$	GPa	7.58	6.89	6.55	4.07	24.1
	Msi	1.1	1.0	0.95	0.590	3.5
$\nu_{LT} = \nu_{xy}$		0.32	0.31	0.39	0.67	0.30
$\nu_{TZ} = \nu_{yz}$		0.32	0.25	0.35	0.01	0.30
$\nu_{LZ} = \nu_{xz}$		0.32	0.25	0.32	0.02	0.30
$G_{LT} = G_{xy}$	GPa	3.45	4.58	4.14	0.0203	9.28
	Ksi	500	664	600	2.95	1346
$G_{TZ} = G_{yz}$	GPa	3.10	1.28	3.72	0.150	9.28
	Ksi	450	185	540	21.8	1346
$G_{LZ} = G_{xz}$	GPa	3.10	1.28	3.72	0.220	9.28
	Ksi	450	185	540	31.9	1346
ρ	g/cc	1.714	1.714	1.714	0.153	2.062
	lb/in^3	0.0619	0.0619	0.0619	0.00551	0.0745
t	mm	0.571	0.457	0.203	9.53	19.1
	in	0.0225	0.018	0.008	0.375	0.75

Table 1: Material parameters for principal directions in the fiberglass layup. Parameters correspond to fabric layers in a material layup with 40% fiber volume. The x element-coordinate represents the longitudinal (L) direction of the fabric; the y element-coordinate represents the transverse (T) direction in the plane of the fabric; and the z element-coordinate represents the transverse (Z) direction perpendicular to the plane of the fabric.

		Layup Material		
		A130 (0's)	D155 (0's)	DB120 (±45's)
$\varepsilon_L = \varepsilon_x(\%)$	tension	2.53	2.83	2.49
	compression	-0.92	-2.02	-2.08
$\varepsilon_T = \varepsilon_y(\%)$	tension	0.39	0.30	0.33
	compression	-1.05	-1.67	-1.21

Table 2: Ultimate strains for principal directions in the fiberglass layup. The x & y element-coordinates respectively correspond to the longitudinal (L) & transverse (T) fiber directions.

3 Static Behavior

Analogous to the design of a laminated wood epoxy (LWE) blade, the composite (GRP) blade was designed to be stiff in character, i.e., relative to the tower. The stiffness parameters of the GRP blade were compared to estimates that were available for the LWE blade design. This section presents a set of these flexural and torsional evaluations.

To obtain these stiffness estimates with the finite element model, the blade was treated as a cantilever beam. All degrees of freedom were fixed in the root plane (11 inches from the center of rotation) and the loads were then applied at the extreme tip of the blade. The material at tip of the blade was modeled with relatively stiff properties to account for the structural buildup associated with tip brake attachments.

The rigidity of the blade was evaluated in terms of three distinct components: flapwise, edgewise, and torsional rigidity. The modeling techniques and corresponding results for each of these components is presented in the following discussion.

3.1 Flexural Rigidity

In general, there are two issues of concern that are tied to the flexural rigidity in the design of a blade. The primary concern is associated with the dynamic behavior of the blade under periodically varying load conditions, such as gusting winds. The second concern is tower strikes. If the blade is not sufficiently rigid in the flapwise direction, the probability of a blade striking the tower and destroying itself under gusty wind conditions increases significantly. Because the LWE blade design has performed in a satisfactory manner with regard to both of these concerns, the initial stage of the design process was focused designing the GRP blade with a flexural rigidity that was similar to that of the LWE blade, particularly in the flapwise direction.

The *flexural rigidity* can be defined as the ratio of the bending moment (M) that is transmitted across a given cross section to the corresponding rate of cross sectional rotation (θ) per unit length (z). Mathematically, the flexural rigidity can be expressed as

$$\frac{M}{d\theta/dz} = EI, \qquad (1)$$

where E represents the effective elastic modulus and I represents the effective moment of inertia. For a prismatic bar with isotropic material properties, the effective elastic modulus (E) and moment of inertia (I), and hence the flexural rigidity (EI) can be determined quite readily (Gere and Timoshenko, 1997; Popov, 1990). For a multicell cross section with layered non-isotropic material properties, the expression for the flexural rigidity is not so easily determined. However, with a finite element model, it is possible to "back-out" estimates using nodal forces and displacements from the solution.

For this study, the moment (M) acting on a given cross section was determined from the forces acting on the nodes in that cross section of the finite element model. Then the rate of rotation ($d\theta/dz$) was determined from the equilibrium positions of the nodes after loading. In particular, the angle of rotation (θ) was approximated by assuming that the cross section geometry and hence the reference line length remained constant under loading. The reference line length (L) was then used to define two equal length sides of a triangle. The remaining side was defined as the length of the displacement vector that was defined by taking the magnitude of the difference of the displacements ($u_1 - u_2$) of the nodes used to define the ends of the reference line (Figure 4a). In essence, this procedure was used to shift the displaced reference line so that one of the endpoints coincided with the endpoint of the original reference line (Figure 4b). With the resulting triangle, the angle of rotation (θ) was then determined via the law of cosines.

The angle of rotation was recorded for each plane of nodes along the length of the blade. This data was then used to construct a piecewise linear function for the angle of rotation (θ) as a function of the span-wise coordinate (z). The rate of rotation ($d\theta/dz$) was then determined by taking the first order finite difference of the bending angle with respect to the span-wise coordinate (z).

For bending in the flapwise direction, a line perpendicular to the chord line was used as a reference for bending-type displacements. For edgewise bending rigidity the chord line was used as the reference line.

3.1.1 Flapwise Rigidity

To study the flapwise bending rigidity of the composite blade, a total force of 1,000 lb was applied to the tip of the blade as displayed in Figure 5a. The corresponding deformed geometry is displayed in Figure 5b. For a 1,000 lb tip load, the GRP blade tip displaced 22.2 inches in the flapwise direction. The flapwise bending angle (θ) is displayed in Figure 5c as a function of z. The corresponding rate of bending ($d\theta/dz$) is graphed in Figure 5d, also as a function of z. The resulting estimates for the bending stiffness (EI) are displayed in Figures 5e and 5f. The spurious

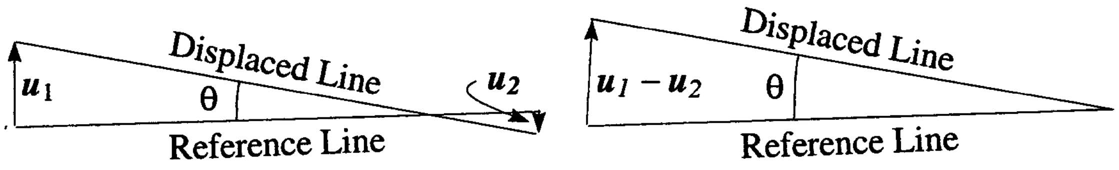

(a) rotation and displacement

(b) rotation-angle (θ)

Figure 4: Geometric measure of rotation/twist under load

responses near the blade tip ($z = 295$ in) are due to the stiffness discontinuity in the model between the thin blade-skin laminate and the three quarter inch thick aluminum tip-brake plate where the flapwise loads were applied. The actual design will include internal filler material to transmit braking loads to the blade-skin laminate in a more even fashion. For the present study, the spurious responses near the tip were ignored.

To provide a comparison, the flapwise flexural rigidity of both the LWE and GRP blade designs are plotted together in Figures 5e and 5f. The values for the flexural rigidity of the LWE blade are based on estimates calculated by Zuteck (1996). Notice that the flapwise rigidity of the GRP blade design is approximately equal to, though slightly less than, the rigidity of the LWE blade design. This approximate match in flapwise stiffness was obtained only after several iterations in layup definitions. A more exact match was not considered essential, with a range of additional criteria left to consider.

3.1.2 Edgewise Rigidity

To analyze the edgewise bending stiffness of the composite blade, a total force of 1,000 lb was applied to the tip of the blade as displayed in Figure 6a. The corresponding deformed geometry is displayed in Figure 6b. For a 1,000 lb load, the tip displaced 5.0 inches.

The bending angle (θ) corresponding to a 1,000 lb edgewise tip load is displayed as a function of z in Figure 6c. The corresponding rate of bending ($d\theta/dz$) is graphed in Figure 6d, also as a function of z. The resulting estimates for the bending stiffness (EI) are displayed in Figures 6e and 6f.

To provide a means of comparison, the values for the edgewise flexural rigidity of the LWE and GRP blade designs are plotted together (Figures 6e and 6f). The values for the flexural rigidity of the LWE blade are based on estimates calculated by Zuteck (1997a). Notice that the edgewise rigidity of the GRP design is substantially ($\sim$70%) less than that of the LWE design. According to Zuteck (1997a), the LWE blade was over designed with respect to edgewise stiffness because of manufacturing constraints. Because the LWE blade was viewed as having a higher than necessary rigidity in the edgewise direction, the difference between the LWE and GRP blade designs was not viewed as a serious concern and was instead viewed as an advantage that would lead to a decrease in costs associated with material and weight.

3.2 Torsional Rigidity

Though torsional rigidity was viewed as a lesser concern and was not considered a design driver, it was evaluated for the sake of completeness. The associated analysis techniques and results are presented in the following discussion.

The *torsional rigidity* is defined as the ratio of the torque (T) that is transmitted across a given cross section to the corresponding rate of twist (θ) per unit length (z). Mathematically, the torsional rigidity can be expressed as

$$\frac{T}{d\theta/dz} = JG, \tag{2}$$

where G represents the effective shear modulus and J represents the effective polar moment of inertia. For a cylindrical bar with isotropic material properties, the effective shear modulus (G) and polar moment of inertia (J), and hence the torsional rigidity (JG) can be determined quite readily (Gere and Timoshenko, 1997; Popov, 1990). For the GRP blade design, the torsional rigidity was "backed-out" using the technique discussed above (§3.1). In this case, the chord line was used as the reference line.

To estimate the torsional rigidity of the composite blade, a force couple of 10,000 in lb was applied to the tip of the blade as displayed in Figure 7a. Based on the linear elastic model, under this applied torque the blade twisted approximately 6.1 degrees at the tip, as displayed in Figure 7b.

For a 10,000 in lb torque, the angle of twist (θ) is displayed in Figure 7c as a function of z (along the length of the blade). The corresponding rate of twist ($d\theta/dz$) is recorded in Figure 7d, also as a function of z. Then the resulting estimates for the torsional stiffness are displayed in Figures 7e and 7f.

Unfortunately, there were no estimates available for the torsional rigidity of the LWE blade design. Because these estimates were unavailable for comparison, the GRP torsional rigidity estimates are relatively meaningless. However, the torsional rigidity estimates for the GRP design are presented here with the assumption that they may be useful at some point in the future.

3.3 Discussion

In summary, in the flapwise direction, the modeled GRP design is nearly but not quite as stiff as the LWE design. The differences are small enough that the probability of tower strikes should be acceptably low, based on experience with the LWE blades. Also, because the LWE and GRP blade designs are relatively similar, in terms of flapwise stiffness, they should have comparable flapwise natural frequencies. Again, because the LWE blades have performed in a satisfactory manner in terms of dynamic responses, it is reasonable to expect that the GRP blade will behave in a similar manner under flapwise loads.

In the edgewise direction, the GRP design is approximately 30% as stiff as the LWE design. These results were considered suitable as tower strikes are not a concern in the edgewise direction. However, the difference could lead to unexpected dynamic responses under periodic edgewise loads. An evaluation of concerns related to dynamic behavior is presented in the following section.

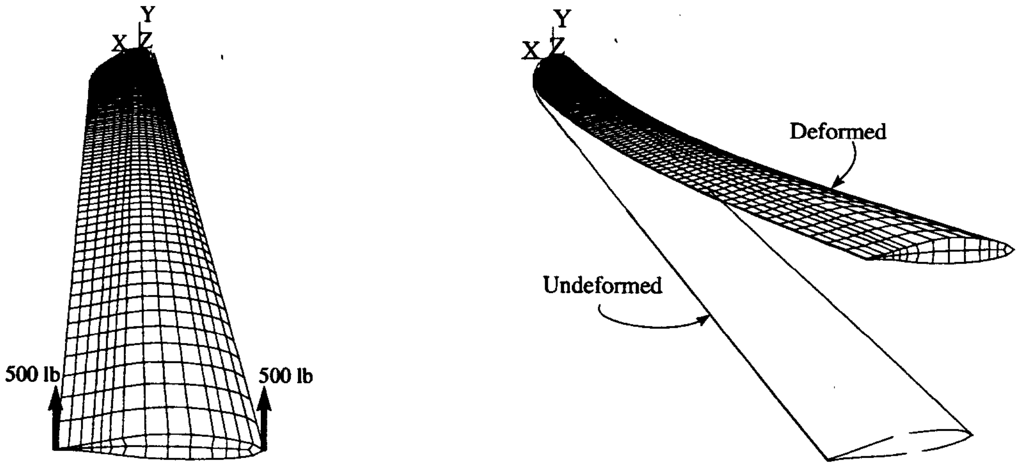

(a) Application of 1,000 lb tip load

(b) Deformed geometry

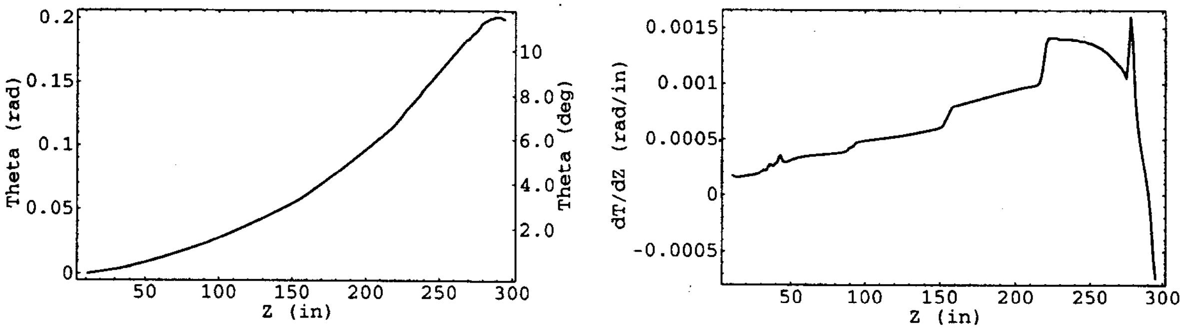

(c) Bending angle

(d) Bending rate per unit length

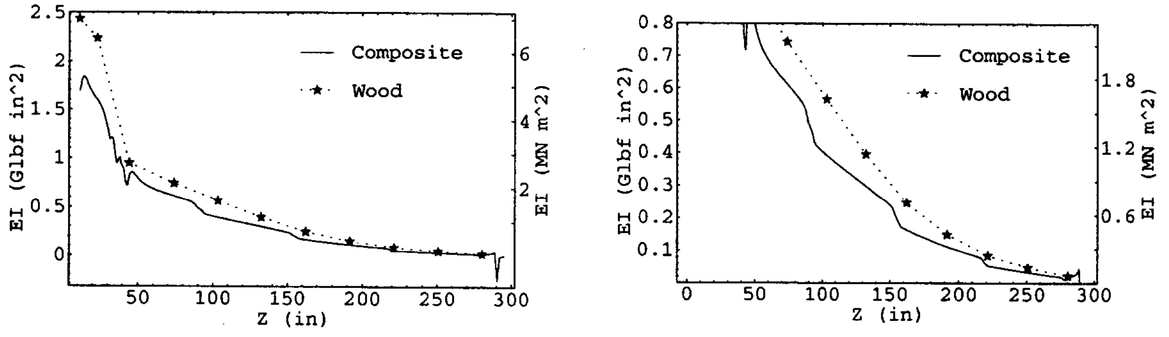

(e) Bending stiffness (entire blade)

(f) Bending stiffness (outboard of root)

Figure 5: Flapwise rigidity of the LWE and GRP blade designs. For a tip load of 1,000 lb, the GRP blade tip displaced 22.2 inches with a cross-sectional rotation of 11.4°, indicating a mean flexural rigidity of 0.41 Glbf in^2 in the flapwise direction.

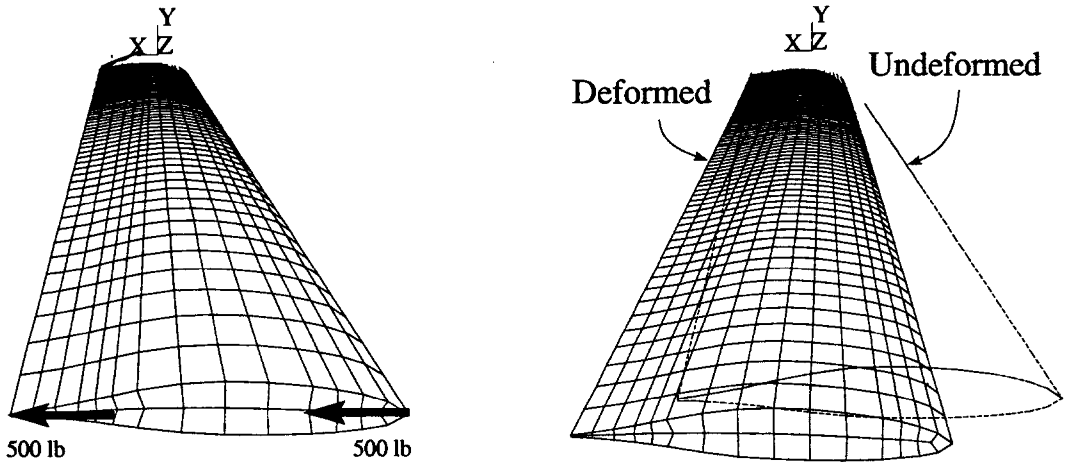

(a) Application of 1,000 lb tip load

(b) Deformed geometry

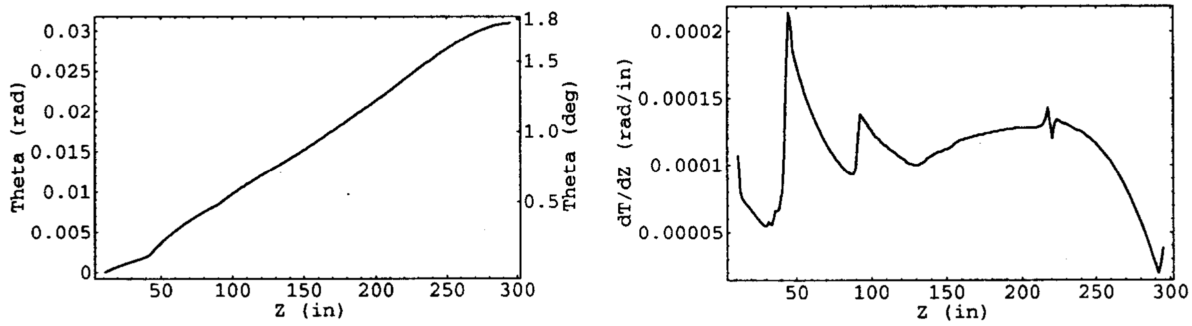

(c) Bending angle

(d) Bending rate per unit length

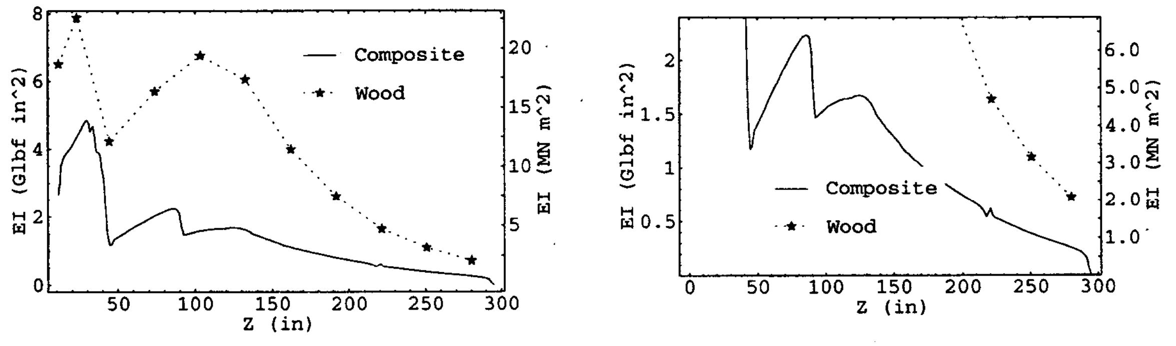

(e) Bending stiffness (entire blade)

(f) Bending stiffness (outboard)

Figure 6: Edgewise rigidity of the LWE and GRP blade designs. For a tip load of 1,000 lb, the GRP blade tip displaced 5.0 inches with a cross-sectional rotation of 1.8°, indicating a mean flexural rigidity of 2.6 Glbf in^2 in the edgewise direction.

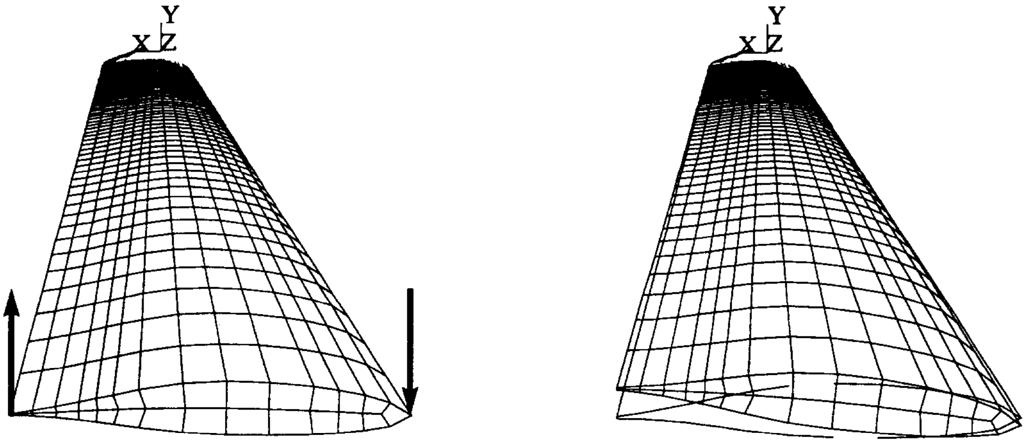

(a) Application of 10,000 in lb torque

(b) Deformed geometry

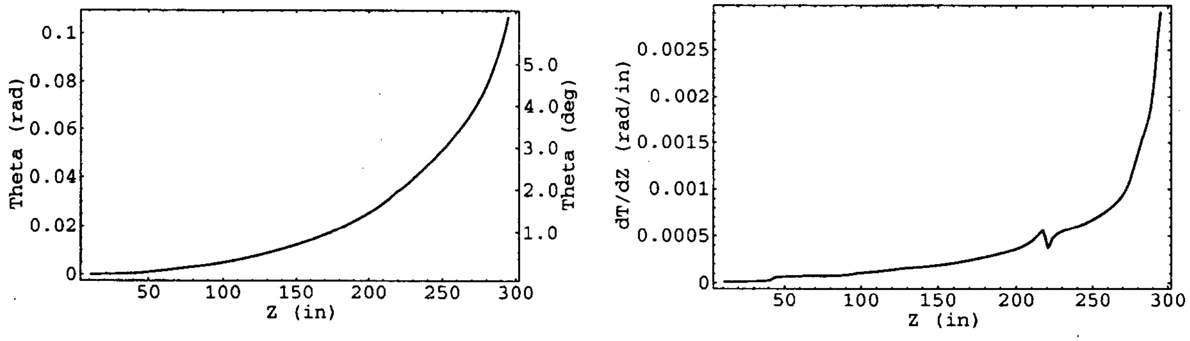

(c) Twist angle

(d) Twist rate per unit length

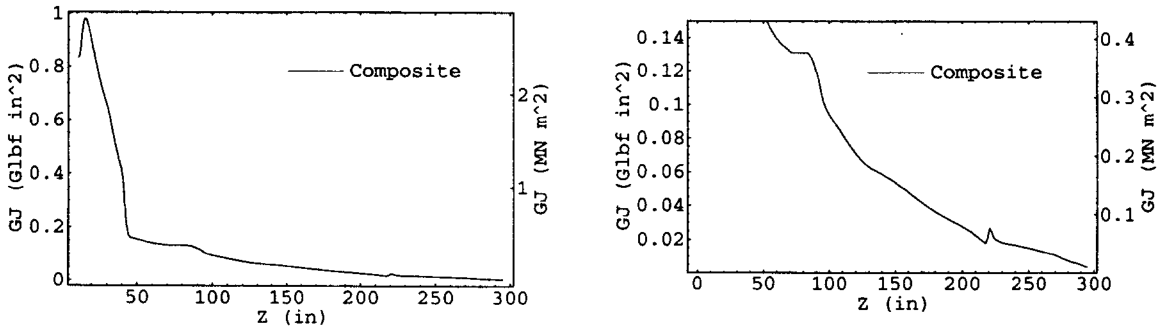

(e) Torsional Stiffness (entire blade)

(f) Torsional stiffness (outboard)

Figure 7: Torsional rigidity of the GRP blade design. For a torque of 10,000 in lb, the GRP blade tip twisted 6.1°, indicating a mean torsional stiffness of 0.027 Glbf in^2.

4 Dynamic Behavior

One feature of interest in the analysis of a dynamically loaded structure is the harmonic frequencies of free vibration for the structure, as excitations at or near these frequencies can generate large structural displacements and, as a consequence, large stresses and strains. These natural frequencies are dependent on the fundamental characteristics of the structure, such as geometry, density, and stiffness. Because these same characteristics can be included in an FE model of a structural component, the FE model can be used to determine the natural modes of vibration and corresponding frequencies.

Once the geometry, density, and elastic material models have been defined for the FE model, in the absence of damping, which can be factored in later, the dynamic character of the model can be expressed in matrix form as

$$[K]\{u_i\} = \omega_i^2 [M]\{u_i\}, \tag{3}$$

where $[K]$ is the stiffness matrix, $[M]$ is the mass matrix, ω_i is the circular frequency of vibration (eigenvalue) for a given mode and $\{u_i\}$ is the mode (eigen) vector that expresses the corresponding mode shape. The finite element program simply uses iterative techniques to determine a set of frequencies and shapes that satisfy the FE matrix equation.

4.1 Harmonic Modes

Because the blade receives dynamic loads both while it is spinning and while it is stopped[4], both cases were considered. For a blade on a stopped rotor, gravitational effects were neglected and the blade was modeled in an unstressed state. To simulate a spinning rotor, gravitational effects were again neglected, but the blade was subjected to a prestressed inertial load state that would result from a constant rotational velocity of 65 RPM. In both cases, the blade was assumed to be rigidly attached to the hub of the turbine at the root end of the blade.

The first five modeled mode shapes and natural frequencies, with the rotor spinning and the tip brake weight set to 18 lbs, are shown in Figure 8. For the spinning blade model with the tip brake weight set at 18 lb, the fundamental flapwise and edgewise vibrational modes occurred at frequencies of 3.9 and 7.3 Hz, respectively. For a stopped rotor, the fundamental flapwise and edgewise vibrational modes occurred at frequencies of 3.6 and 7.2 Hz, respectively (Table 3). Other vibrational modes occurred at frequencies above 13 Hz.

Though the combined weight of tip brake and the required attachments is expected to be approximately 18 lbs, the combined weight is still relatively undefined. Therefore the combined

---

[4] When wind speeds exceed 22.4 m s^{-1} (50 MPH), wind speed sensors simultaneously activate tip and hub brakes that bring the rotor to a stop. Once the rotor is stopped, the hub brake holds the rotor in a *stopped* state and prevents it from spinning until the wind speed drops to an acceptable level. However, the turbine, and hence the rotor, is still free to yaw about the vertical tower-axis in this stopped state.

weight of the tip brake and its components was varied to evaluate the possible significance of such changes. As shown in Table 3, as the tip brake weight was varied by ±2 lb, the fundamental flapwise and edgewise frequencies varied by approximately ±0.1 and ±0.2 Hz, respectively.

The frequencies presented in Table 3 compare well with frequencies reported for the wood blade. For the wood blade, Johnson (1996) reports that for a locked rotor, the first flapwise natural frequency was 3.75 Hz and for a rotor spinning at 65 RPM, the first flapwise natural frequency was 3.9 Hz. For a stopped rotor, experimental data is also presented in Rumsey et al. (1998) and Gross et al. (1999).

To validate the results with simple hand calculations, because the blades were firmly attached at the root and were otherwise free to deform under load, the blade vibrations could be modeled, in an approximate manner, using a cantilevered beam model. For a prismatic beam, the first natural frequency (f_1) can be modeled by

$$f_1 = \frac{1.875^2}{2\pi l^2}\sqrt{\frac{EI}{m}}, \tag{4}$$

where l is the length of the beam (Blevins, 1977, Tab.8-1).

Using mean values for the flexural rigidity and mass per unit length, this beam model indicates that the first natural frequency of the blade is ~2.9 Hz, indicating that the finite element estimate of ~3.7 Hz was reasonable given the approximate nature of the beam model for the non-prismatic blade geometry.

In general, the modal frequency estimates presented above seem reasonable. However, the question remains as to what periodic-type loads may act on the blades and what the likelihood is that these loads will induce a resonant response from the blades. Those who have worked in the wind turbine industry for any length of time know that this is a ticklish issue for the designer. The following discussion addresses only a small set of the more obvious sources of periodic-type excitations; other sources will be considered as research progresses.

4.2 Periodic Excitations

For a wind turbine blade, periodic excitations can be generated by several sources. One source of periodicity is related to the constant rotational speed (~65 rpm) of the turbine rotor. This constant rotational speed translates any spatial variations in the wind throughout the rotor's span into periodic blade loads as the blade passes through each complete rotation.

In particular, for HAWT's such as the AOC 15/50, the wind load typically varies with height due to boundary layer effects imposed by the ground. In this case the wind load will be a minimum at the bottom of each rotational cycle and a maximum at the top of each cycle. Additionally, for downwind HAWT's, the tower will generate a wake, often referred to as a *tower shadow*, through which the blade passes at the bottom of each rotation. This tower-shadow often yields a significant decrease in the wind load. Consequentially, variations in gravitational loads, ground effect, and the tower-shadow effect can combine to yield significant periodic variations in the bending loads.

For a spinning rotor, excitable frequencies occur as integer multiples of the rotor's per-revolution (P) frequency (Sullivan, 1981). As displayed in Figure 9, a Campbell diagram can be used to evaluate possible interactions between these excitation frequencies and the natural frequencies of the different structural components.

In Figure 9, the lines radiating from the origin represent possible excitation frequencies as the rotor spins up to its operating speed. The vertical line at 65 RPM represents the standard operating speed for the AOC 15/50 wind turbine. The fundamental natural frequencies for the tower and the blades are then illustrated as horizontal curves that, for the blades, increase gradually with increasing rotational speed[5]. Resonance is likely to occur at points where excitation frequency curves and natural frequency curves cross one another. Based on this Campbell diagram (Figure 9), resonance is not likely at the standard operating speed of 65 RPM.

A second excitation source is associated with tower vibrations. As the tower sways in the wind, the blades must follow. If the blades have a natural frequency that can be excited by the inertial response associated with such periodic movements, tower-blade interactions can lead to modal responses with large structural displacements and hence large strains.

For the standard AOC lattice tower with a turbine using LWE blades, the fundamental natural frequency has been recorded at 1.67 Hertz (Gross, 1999, Tab.5-1). Because this first tower frequency is significantly higher than the rotor frequency (~1.1 Hz), the tower is not likely to be excited by periodic variations in rotor loads. However, the tower vibrations can be induced by gusting winds. In such a case, with GRP blades, the top of the tower is expected to sway with a frequency on the order of ~1.6 to 1.7 Hz. Because this can occur when the rotor is spinning or stopped, both cases must be considered. This implies that a blades' fundamental natural frequency may vary between 3.5 and 4 Hz (Table 3). For a frequency near 4 Hz, interaction is likely to be minimal; however, as the first natural frequency for a stopped rotor approaches ~3.4 Hz, twice the first tower frequency, the likelihood of interaction and hence magnified displacements increases. Though not large enough to damp out oscillations at a major resonance, aerodynamic drag serves as a significant source of damping when the blade vibrates in the flap-wise direction, reducing the amplifying effect of tower-blade frequency interaction.

---

[5] Reviewers indicate that frequencies typically rise in a more significant fashion with increasing rotor speeds. As a consequence, though modeled results correspond to measured results for the LWE blade (Johnson, 1996), there is some doubt regarding the validity of the results for a spinning blade (Figure 9).

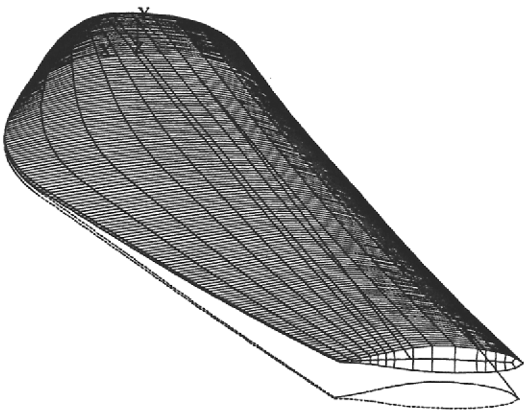

(a) 1st mode (flap-wise)

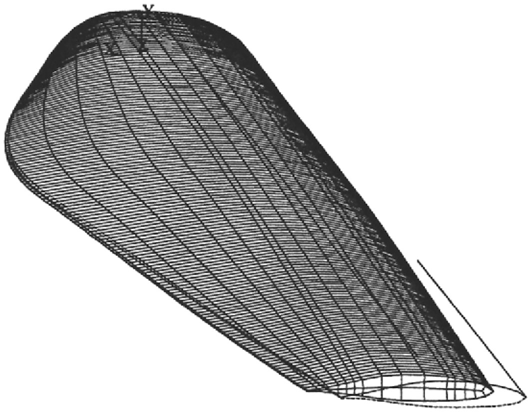

(b) 2nd mode (edge-wise)

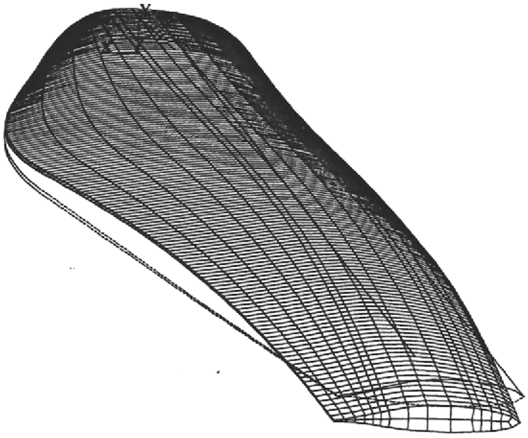

(c) 3rd mode (flap-wise)

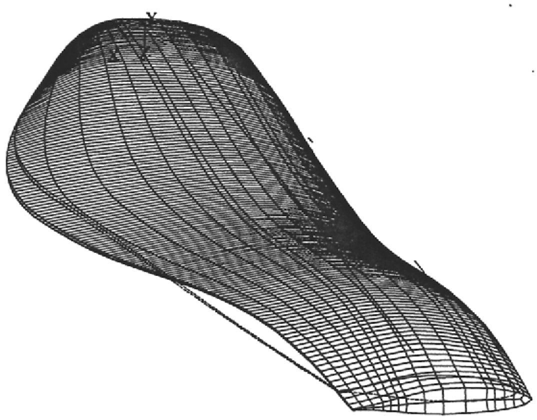

(d) 4th mode (flap-wise)

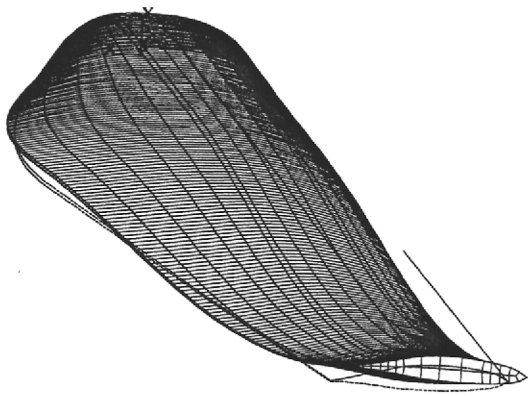

(e) 5th mode (mixed)

Mode Shape	Frequency (Hertz)
1st mode, flap-wise (a)	3.9
2nd mode, edge-wise (b)	7.3
3rd mode, flap-wise (c)	13.9
4th mode, flap-wise (d)	30.2
5th mode, mixed (e)	33.4
Blade Mass	235 lb

(f) Frequency Summary

Figure 8: Mode shapes and frequencies for the modeled blade spinning at 65 RPM. Nodes were fixed at the root and the the tip brake weight was set to 18 lbs.

	Frequency (Hertz)					
	tip brake = 16 lb		tip brake = 18 lb		tip brake = 20 lb	
Mode Shape	spinning rotor	stopped rotor	spinning rotor	stopped rotor	spinning rotor	stopped rotor
1st mode, flap-wise (a)	4.0	3.7	3.9	3.6	3.8	3.5
2nd mode, edge-wise (b)	7.5	7.4	7.3	7.2	7.2	7.0
3rd mode, flap-wise (c)	14.1	13.8	13.9	13.6	13.8	13.5
4th mode, flap-wise (d)	30.4	30.2	30.2	29.9	29.9	29.6
5th mode, mixed (e)	33.7	33.6	33.4	33.2	33.1	32.9
Blade Mass	234 lb		236 lb		238 lb	

Table 3: Natural frequencies for mode shapes (shown in Figure 8). Tip brake weights were varied for cases where the rotor was spinning or locked down.

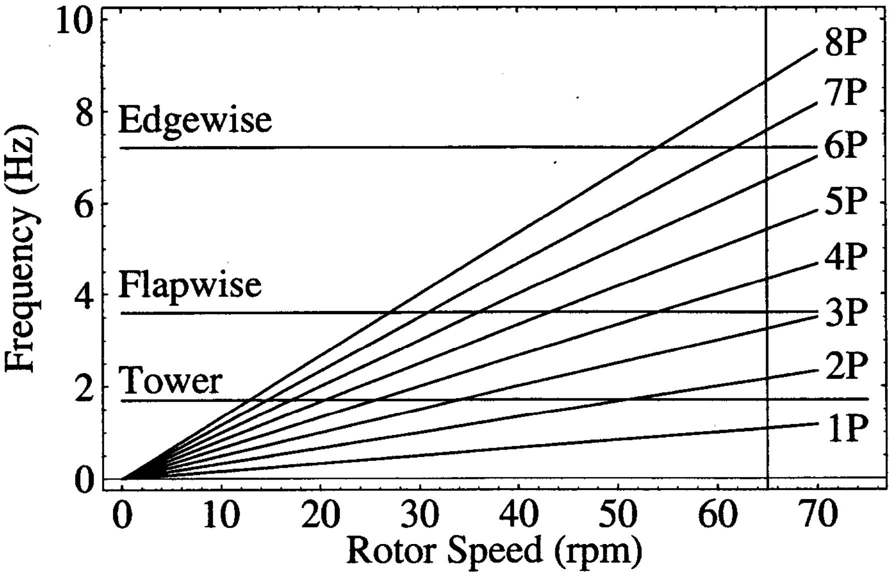

Figure 9: Campbell diagram for the AOC 15/50 turbine with the composite blade design. Intersections indicate resonance crossings, where radial lines from the origin represent potential excitation frequencies due to varied rotor speeds [After Thresher et al. (1994, Fig.11-6)]. The vertical line at 65 RPM represents the standard operating speed.

4.3 Discussion

In summary, for the modeled GRP blade design, the first flap-wise vibrational mode is expected to occur at a natural frequency of ~3.6 Hz with a stopped rotor and ~3.9 Hz with the rotor spinning at 65 RPM. These estimates compare quite well with design estimates for the wood blade, for which the first flap-wise vibrational mode occurs at a natural frequency of ~3.7 Hz with the rotor stopped and ~3.9 Hz with the rotor spinning at 65 RPM. However, as the weight of the tip brake hardware increases, the natural frequencies for the GRP modal responses decrease and diverge from the frequencies for the LWE design. As a consequence, as long as the weight of the tip brake and the associated attachment hardware is minimized, the composite blade can be expected to yield responses to dynamic loads in the flap-wise direction that are quite similar to responses from the laminated wood blade design. More importantly, as long as the tip brake weight is minimized, resonant responses from the GRP design are unlikely—at least for those sources of excitation that were considered.

5 Loads

Wind turbines are, by necessity, installed in areas that have relatively consistent and often strong winds. As a result, wind loads are one of the dominant concerns with regard to the structural behavior and life of a wind turbine blade. Wind loading conditions can be divided into two classes: (1) Operating conditions, where the turbine rotor is spinning; and (2) extreme wind conditions, for which the turbine is not operating. Extreme wind conditions can shorten the life of a wind turbine blade in a rather drastic fashion. Operating loads typically play a significant role in the fatigue life of a blade.

To model either condition and the load that it places on each individual blade requires an evaluation of the relative velocity of the wind as it approaches the blade and the manner in which it varies with time. As discussed in Frost and Aspliden (1994), wind speeds (v) that vary with time (t) are commonly divided into a steady component ($\bar{v}$) and a non-steady component (v') as follows:

$$v(t) = \bar{v} + v'(t), \tag{5}$$

where

$$\bar{v} = \frac{1}{\Delta t}\int_0^{\Delta t} v(t)dt \qquad \text{and} \qquad \int_0^{\Delta t} v'(t)dt = 0. \tag{6}$$

Notice that the magnitude of the steady or mean component of velocity ($\bar{v}$) is often dependent on the size of the averaging interval of time (Δt). The rate of change of the non-steady gusting component then plays a role in the dynamic interaction between the structure and the local air stream.

When a fluid moves relative to a structural object, the moving fluid (i.e., wind) exerts force (F_W) that is approximately proportional to the square of the fluid velocity (v), i.e.,

$$F_W = Cv^2, \tag{7}$$

where the constant of proportionality (C) is referred to as a shape factor and is often determined experimentally (Sachs, 1978, §1.2). For semi-aerodynamic and aerodynamic shapes, such as wind turbine blades moving into the wind, the shape factor varies with fluid velocity (v) and can be expressed as a function of the Reynolds number (R_e). For non-aerodynamic shapes, such as wind turbine blades turned perpendicular to the wind, the shape factor is essentially constant.

In the discussion that follows, wind loads are modeled as statically equivalent loads where the steady load will be modeled as an applied pressure and the dynamic effect of the non-steady component will be included as a load multiplier.

5.1 Operating Conditions

For standard operating conditions, as the rotor spins at 65 RPM, the tip of each blade moves at a velocity of 113 mph (51 m s^{-1}). If the driving wind is temporarily ignored and the rotational effect is considered individually, the relative wind velocity in the edgewise direction varies between 113 mph and zero at the hub. At the same time, under standard operating conditions, the driving wind (presumably in the flapwise direction) can vary between the cut-in velocity of 10.2 mph (4.6 m s^{-1}) and the shutdown velocity of 50 mph (22.4 m s^{-1}).

At the shutdown velocity (50 mph), the sum of the rotational component and the driving component yields a velocity of ~125 MPH (55.7 m s^{-1}) that approaches the blade at a 24° angle relative to the plane of rotation. Near the hub of the rotor, the rotational component is zero and the relative wind approaches perpendicular to the plane of rotation at a velocity of ~50.1 MPH (~22.4 m s^{-1}). At the cut-in velocity (10.2 MPH), assuming the blade has reached its rotational speed of 65 RPM, the sum of the rotational component and the driving component yields a relative velocity of ~115 MPH (51.2 m s^{-1}) that approaches the blade at a 5° angle relative to the plane of rotation. Near the hub of the rotor, the rotational component is zero and the relative wind approaches perpendicular to the plane of rotation at a velocity of 10.2 mph. Clearly, operating loads can vary significantly as relative wind velocities vary between these two extremes.

Because the magnitude and direction of the relative wind velocity vary so drastically along the length of an operating blade, operational loads are not easy to define. Also, because these operating loads are smaller than those imposed by extreme wind conditions, they were not considered a driving component in the initial design phase. As a consequence, operating loads were not modeled in the present study and will therefore not be discussed further in this report but will instead be considered as a subject for further study.

5.2 Yaw Induced by Extreme Wind Shear

The term *wind shear* refers to variations in the wind velocity that occur over distances that are on the order of meters. If wind shear develops between the right- and left-hand edges of the rotor (a likely case under gusty conditions), the resulting pressure-load differential generates a moment about the vertical axis. Because the AOC 15/50 is a free-yawing wind turbine (i.e., free to rotate about the vertical tower-axis), a moment about the vertical axis induces rotation. Rapid rotations about the tower axis put the blades into a range of bending modes that vary depending on the position of the individual blade and the yaw rate or yaw acceleration.

To study yaw effects resulting from extreme wind shear, data was collected from a Palm Springs site and was used as input for an ADAMS FE model of the AOC 15/50 wind turbine with wood blades (Johnson, 1996). Yaw rates and accelerations from this analysis are displayed in Figure 10. Based on these results, combined with the assumption that the rotational inertia of the composite blades will be similar to that of the wood blades, it is reasonable to expect extreme yaw rates on the order of 45 deg s^{-1} and extreme yaw accelerations on the order of 470 deg s^{-2}.

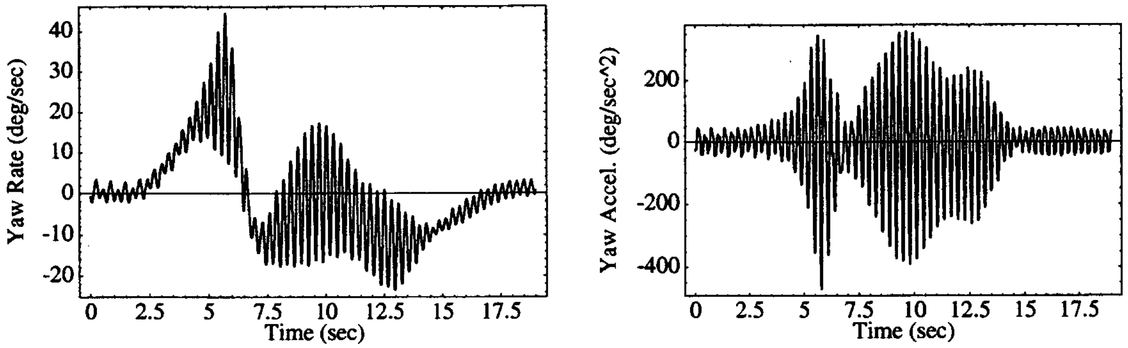

(a) Yaw velocity

(b) Yaw acceleration

Figure 10: Yaw estimates based on blade data taken from Palm Springs (Johnson, 1996). The maximum yaw rate is 45 deg s^{-1} and the maximum yaw acceleration is 470 deg s^{-2} .

5.3 Extreme Wind Speeds

For the AOC 15/50 wind turbine, the GRP blade was designed to survive an extreme wind speed of 133 MPH. To withstand a 133 MPH wind, the blade must be able to survive a category 3 hurricane on the Saffir-Simpson scale (Liu, 1991, Tab.1-2). Damage associated with category 3 hurricanes is typically rather extensive, where foliage is torn from trees and large trees are blown down. Often any poorly constructed signs will be blown down and roofing materials and doors on buildings will be damaged. In addition, there will be some structural damage to small buildings and many mobile homes will be destroyed.

To model the blade load for a stationary wind turbine due to such extreme winds, the dynamic pressure on the high pressure side of the blade was modeled as

$$P_{hp} = \frac{1}{2}\rho v^2, \tag{8}$$

where ρ is the air density and v is the wind velocity. For a 133 MPH wind, the stagnation pressure (P_{hp}) becomes 0.314 psi. If the blade is modeled as a flat plate that lies normal to the flow, then the effective pressure differential between the high and low pressure faces of the blade can increase to as much as 140% of the stagnation pressure (Fox and McDonald, 1978, Fig. 8.31). As a consequence, the pressure differential between the high and low pressure sides of the blade can be $\sim$0.44 psi.

However, because such extremes often occur under gusty conditions, the gusts or non-steady components of the wind velocity can occur in a periodic fashion. If the gust frequency is close to the natural frequency of the blade, deflections can become increasingly large. To account for this dynamic interaction, it is often considered acceptable to model the interaction using "statically equivalent loads". In the present case, the applied pressure was increased by an additional 40% to account for possible interactions between the blade and the gusting component of the wind, implying that the effective pressure was 0.62 psi. With this wind load model, the resulting distribution has a total magnitude of ~4200 lbs of force. For the FE model, this load was distributed evenly in the span-wise direction and as a bilinear gradient with the maximum at the quarter chord position in the chord-wise direction[6], as displayed in Figure 11.

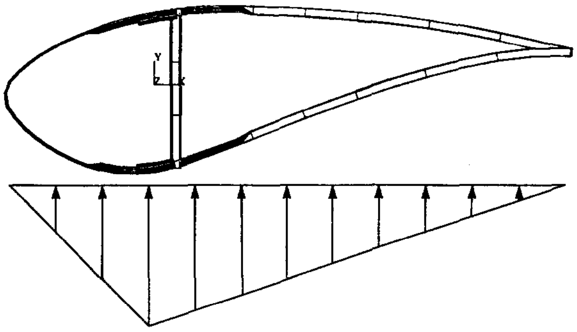

Figure 11: Pressure distribution as applied to the blade model.

Notice that, except for encounters with tornadoes, this wind load model is quite conservative for inland installations. First, if the steady component of 133 MPH is compared with peak gust velocities recorded at one-hundred and twenty stations in the USA (Sachs, 1978, Fig.2.18), the 133 MPH velocity is approximately equal to the maximum of the peak gust velocities. Second, the drag imposed on a flat-wise blade will more than likely be less than that on a flat plate so that a drag factor of 1.4 can be considered conservative. Third, the periodicity of the non-steady wind component is not likely to match the frequency of the blade for an extended period of time, so that a dynamic gust factor of 1.4 can also be considered conservative. However, conditions imposed by a tornado or category 4+ hurricane can rapidly generate loads in excess of the design load.

6 Limiting Load Cases

For the present report, extreme load conditions were considered in some detail while operational load conditions were neglected. As discussed in the previous section (§5), two limiting load conditions of concern were yaw induced by extreme wind shear and wind loads due to extreme wind speeds. These loads were applied to the FE blade model in the manner discussed previously (§5.2-5.3). The model's response to these loads is discussed in the following sections.

---

[6] There was some debate regarding the selection of the bilinear pressure distribution in the chord-wise direction. However, test cases discussed later in the report indicated that variations in the chord-wise distribution resulted in only minor variations in the bending strains (Table 4).

6.1 Yaw Induced by Extreme Wind Shear

As discussed in Section 5.2, the blade's reaction to yaw depends on the position of the blade and the yaw rate or acceleration. For the load cases presented here, the maximum yaw rate of 45 deg s^{-1} and the maximum yaw acceleration of 470 deg s^{-2} were applied independently.

The maximum yaw rate generates a maximum bending load in a blade that is vertical or parallel to the tower. This load develops as the rotor hub, which is ~3 ft from the tower axis, swings about the tower axis. In response to this yawing motion, blades that are directly above or below the hub tend to bend toward the horizontal. The blade above the hub is in the more unstable position as gravitational forces will add to rather than subtract from the bending loads as the blade deforms; however, this gravitational effect would be small for the case considered and was not included in the model.

The maximum yaw acceleration generates a maximum yaw-induced bending load in a blade that is horizontal or perpendicular to the tower. This load develops as the rotor accelerates about the tower axis and the inertia of a horizontally extended blade tends to bend the blade in an attempt to retard the acceleration.

Strain contours for both of these load cases are illustrated in Figure 12. Because the yaw induced loads impose a bending mode on the blade, the primary stresses and strains are in the span-wise (z) direction. In this case, because the stresses vary from ply to ply in the composite laminate, strains, which were relatively consistent from ply to ply, were plotted and used to evaluate structural capacity.

In comparing Figures 12a and 12b, notice that the strains induced by the extreme yaw rate of 45 deg s^{-1} are ~30 to 40% greater than those induced by the extreme yaw acceleration of 470 deg s^{-2}. In either case, the peak strains are well below the failure strains listed in Table 2. Recall (Figure 3) that the predominant (longitudinal) fiber direction in the composite layup is in the span-wise direction. Based on these results, extreme yaw rates and accelerations were not considered a primary concern for the modeled blade design.

6.2 Pressure Loads due to Extreme Wind Speeds

Under the pressure load representing the 133 MPH wind condition (§5.3), the blade is placed into a bending mode. With bending, the blade can fail by either of two processes: 1) material failure due to excessive stresses and/or strains or 2) geometric instability, otherwise known as buckling. Because pressure loads proved to be the dominant of the two limiting load cases, pressure loads were used to evaluate not only material stability but also geometric stability. The following sections present a selected set of results from the FE model of the blade and how these results were used in the design process.

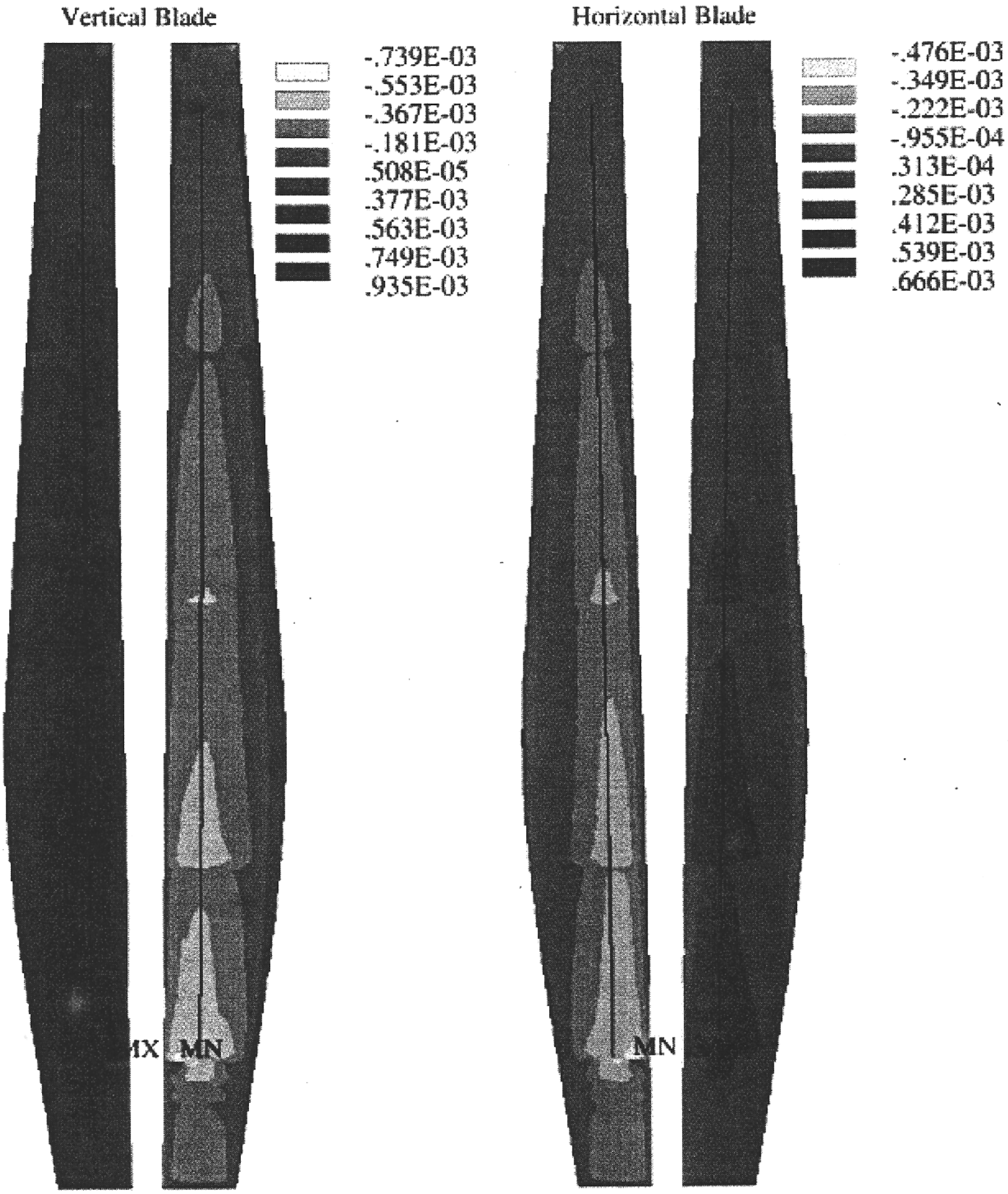

(a) Yaw rate of 45 deg s^{-1} (b) Yaw acceleration of 470 deg s^{-2}

Figure 12: Yaw induced span-wise strains due to extreme wind shear. For cases (a) and (b), the tip displacements were approximately 4.6 and 3.1 inches, respectively.

6.2.1 Bending Strains

For the blade model, the bending load induced by the modeled pressure distribution (Figure 11) yields the strain distributions illustrated in Figures 13 and 14. In nearly every case, the peak strains are concentrated immediately outboard of a major ply drop in the span-wise direction. The highest strains occur on the leading edge at immediately outboard of the root section ply drops and forward (in the chord-wise direction) of the spar cap.

For this load case, the peak strains were significantly higher than the yaw-induced strains. Span-wise strains, i.e., strains parallel to the primary fiber direction, are shown in Figure 13. Comparing these results (Figure 13) with the ultimate strain estimates listed in Table 2, indicates that tensile strains are less than 16% of ultimate and compressive strains are less than 45% of ultimate.

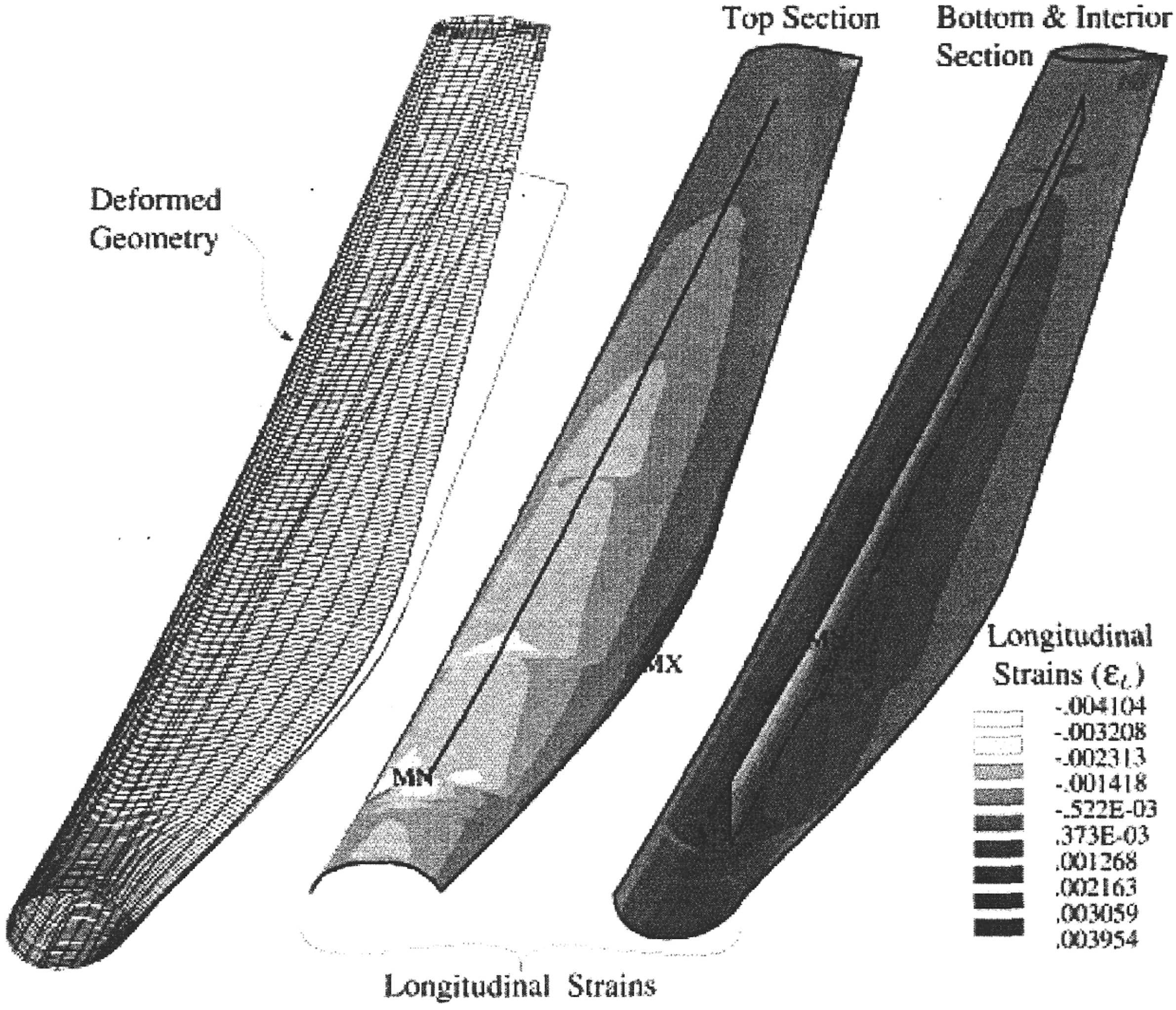

Figure 13: Span-wise (longitudinal) strains due to a 133 MPH wind (~24 in tip displacement).

Assuming linear behavior up to failure—a reasonable assumption for GRP materials—then the applied load would have to be increased by a factor of 2.2 or more to generate compressive failure in the material immediately outboard of the root ply-drops.

The distribution of transverse (chord-wise) strain is illustrated in Figure 14. Again, comparing these strains with the ultimate values provided in Table 2 indicates that tensile strains are less than 55% of ultimate and compressive strains are less than 22% of ultimate. In this case, the modeled pressure load would have to be magnified by a factor of 1.8 or more before the model would indicate probable tensile failure in the transverse direction.

With these results, the peak strain concentration immediately outboard of the root ply-drop region was of some concern; but part of this concentration was due to the rapid manner in which

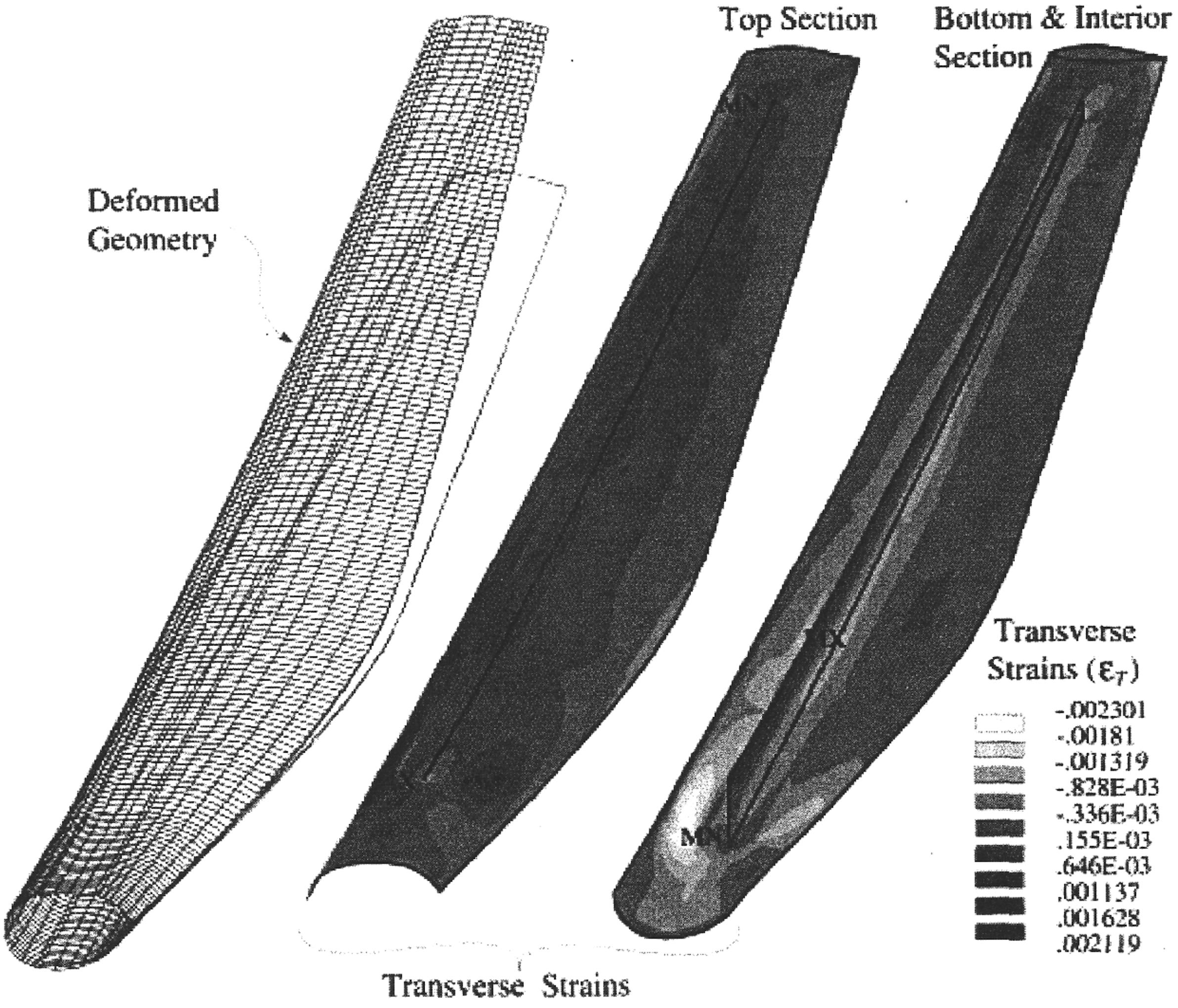

Figure 14: Transverse strains due to a 133 MPH wind load, with a tip displacement of ~24 in.

the plies were dropped in the FE model, i.e., over the width of one element (~2 inches). In the actual layup, the ply drop transition can be extended over a much larger distance with relatively little difficulty. With extended ply-drop transitions, the local strain concentrations can be reduced.

In this analysis, there was some concern over the simplistic nature of the pressure distribution that was used to model the 133 MPH wind condition. To evaluate the significance of the manner in which the pressure was distributed, several different distributions were considered. These distributions were altered only in the chord-wise direction while the distribution in the span-wise direction remained relatively unchanged. For the first case, a constant pressure of 0.62 psi was applied to the high-pressure side of the blade. As a second case, the pressure load was applied with a triangular distribution, with the peak load at the leading edge of the blade (0% of the chord). The three remaining cases were each applied as bilinear pressure gradients that had a peak at an intermediate chord position (25%, 35%, & 45%) and tapered to zero at the leading and trailing edges. The peak strains recorded from these analysis cases are displayed in Table 4.

In Table 4, the first two rows provide a record of the total force and moment at the root connection. The next seven rows are records of the peak strains relative to the predominant fiber direction (x) and where the peak strains occurred. Peak strain locations were recorded both in terms of coordinate location and node number. Locations of key nodes are shown in the blade cross section displayed above Table 4. Notice that this cross section (above Table 4) represents the row of elements where the root ply-drops take place.

Regarding the load cases used to generate Table 4, though the pressure distributions vary significantly, the overall pressure load is relatively unchanged (first two rows). As a consequence, the bending loads near the root are also relatively unchanged; hence the peak strains, which occur near the root region, vary less than 5%. In essence, the results displayed in Table 4 indicate that the choice of pressure distribution plays a relatively minor role in the evaluation of strains due to pressure loads.

Overall, these results indicate that material instability (failure) due to excessive stresses and strains is not expected until the pressure load exceeds the modeled pressure load (133 MPH wind condition) by more than a factor of 1.8. This completes the discussion of material instability; the next issue to be considered is geometric stability, i.e., buckling.

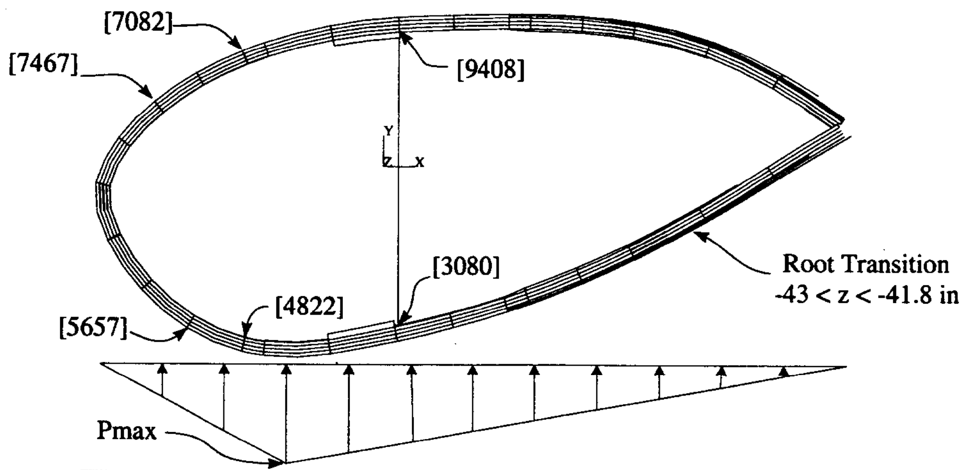

	Const. Pressure	Bilinear Pressure Distribution			
	P = 0.615 psi	Pmax@0%	Pmax@25%	Pmax@35%	Pmax@45%
Flapwise Force @ Root (lbs)	4148	4153	4202	4212	4199
Flapwise Mom. @ Root (in lbs)	571,000	594,000	602,000	605,000	604,000
Max (Tens.) fiber (x) strain {x,y,z} loc	.39% [4822] {−4.2, −5.2, −43.0}	.43% [4822] {−4.2, −5.2, −43.0}	.41% [4822] {−4.2, −5.2, −43.0}	.41% [4822] {−4.2, −5.2, −43.0}	.40% [4822] {−4.2, −5.2, −43.0}
Min (Comp.) fiber (x) strain {x,y,z} loc	−.40% [7082] {−4.2, 3.4, −43.0}	−.38% [7082] {−4.2, 3.4, −43.0}	−.43% [7082] {−4.2, 3.4, −43.0}	−.44% [7082] {−4.2, 3.4, −43.0}	−.45% [7082] {−4.2, 3.4, −43.0}
Max (Tens.) trans (y) strain {x,y,z} loc	.21% [7467] {−6.9, 1.9, −41.8}	.20 [7467] {−6.9, 1.9, −41.8}	.23% [7467] {−6.9, 1.9, −41.8}	.24% [7467] {−6.9, 1.9, −41.8}	.24% [7467] {−6.9, 1.9, −41.8}
Min (Comp.) trans (y) strain {x,y,z} loc	−.24% [5657] {−5.9, −4.9, −41.8}	−.23 [*5741*] {−5.8, −4.8, −44.5}	−.25% [5657] {−5.9, −4.9, −41.8}	−.26% [5657] {−5.9, −4.9, −41.8}	−.26% [5657] {−5.9, −4.9, −41.8}
Max (Tens.) thick (z) strain {x,y,z} loc	.13% [9408] {.43, 4.4, −41.8}	.13% [9408] {.43, 4.4, −41.8}	.14% [9408] {.43, 4.4, −41.8}	.14% [9408] {.43, 4.4, −41.8}	.14% [9408] {.43, 4.4, −41.8}
Min (Comp.) thick (z) strain {x,y,z} loc	−.15% [3080] {.43, −5.2, −41.8}	−14% [3080] {.43, −5.2, −41.8}	−.15% [3080] {.43, −5.2, −41.8}	−16% [3080] {.43, −5.2, −41.8}	−16% [3080] {.43, −5.2, −41.8}
Min (Comp.) shear (xy) strain {x,y,z} loc	.34% [7082] {−4.2, 3.4, −43.0}	.31% [*11150*] {4.4, 4.5, −43.0}	.35% [7082] {−4.2, 3.4, −43.0}	.38% [7082] {−4.2, 3.4, −43.0}	.40% [7082] {−4.2, 3.4, −43.0}
Tip Disp (in)	20.2	22.4	23.2	23.5	23.6

Table 4: Peak strains for varied pressure distributions. Bracketed numbers [] refer to node numbers.

6.2.2 Eigenvalue Buckling

Because extreme wind loads were deemed the most likely cause of blade buckling, the blade model was evaluated for possible buckling modes using the previously discussed pressure distribution (Figure 11). Buckling modes and loads were first evaluated using linear eigen buckling techniques; subsequent, and presumably more accurate evaluations, were completed by considering non-linear geometry often referred to as non-linear buckling models. The results of the eigen buckling models are presented in this section while results of the nonlinear buckling models will be presented in the following section (§6.2.3).

Balsa was included in the trailing edge of the blade primarily to minimize the probability of buckling. Unfortunately, balsa wood comes in flat sections that are not easy to taper. Near the tip of the blade, the blade cross section tapers through the thickness to a point that requires that the thick 3/8" balsa layer be tapered to a thinner thickness (e.g., 1/4") or dropped. To evaluate the possibility of dropping the balsa layer, the balsa was removed from the layup without taper at a position $\sim$219 inches from the rotor hub. The corresponding eigen buckling results are displayed in Figure 15. Notice that the results in Figure 15 indicate that buckling is likely to occur as a distributed pressure load approaches 2100 lbs, 0.49 times the load generated by the modeled pressure distribution—a rather unsatisfactory result.

Following this analysis, the balsa ply-drop was extended to a point 260 inches from the hub center (Figure 3). After extending the balsa ply-drop to the $z = 260$ inch position, buckling was no longer a problem in the trailing edge outboard of the ply drop (see Figure 16). The first two modes in Figure 16 illustrate spurious modes that are presumably due to minor inconsistencies in the node/element definitions used to model the tip brake at the end of the blade. Modes 3 through 5 indicate that the buckling would occur for a distributed load of $\sim 11,000$ lbs, 2.7 times the modeled pressure load.

In both of the previous analyses, balsa was included in the spar to minimize the likelihood of the spar buckling (layup:[$\pm 45/0_2/\pm 45$/balsa/$\pm 45/0_2/\pm 45$] with overall thickness = 0.529 in). To evaluate the significance of balsa in the spar, the balsa was removed and the eigen buckling analysis was repeated. The layup that was used for this case is presented in Figure 3. The results of an eigen buckling analysis with balsa removed from the spar are shown in Figure 17. In this case, the eigen buckling model indicates that buckling will not take place until a distributed load approaches or exceeds $\sim 12,000$ lbs, 2.85 times the maximum expected wind load. In essence, the eigen buckling model indicates that by removing the balsa from the spar layup, the distributed load required for buckling increases[7]. As a consequence, balsa was removed from the layup schedule for the spar.

---

[7] The reason for the increased load capacity, using a blade spar without balsa, is not clear. More than likely, the absence of balsa promotes a more even distribution of strain in the spar cap and hence a more even distribution in the pressure faces of the blade.

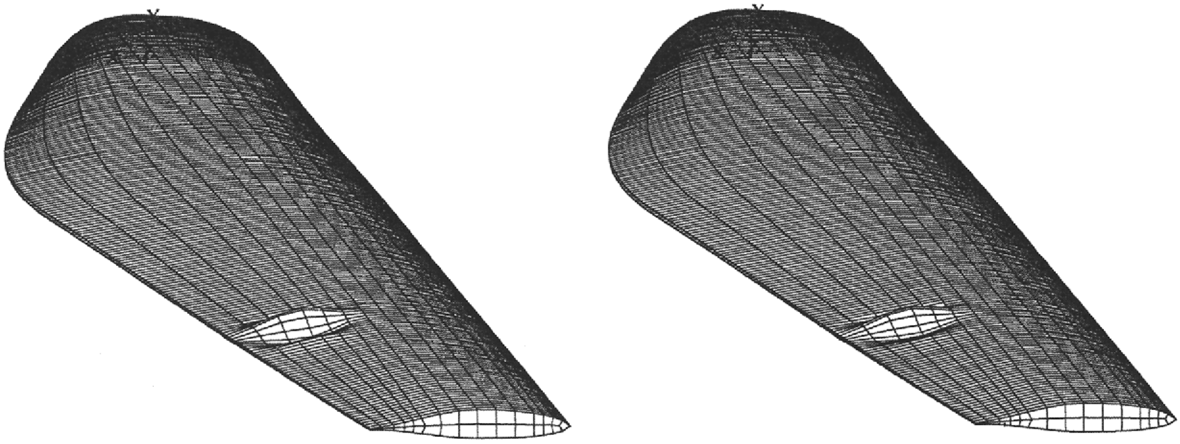

(a) 1st mode

(b) 2nd mode

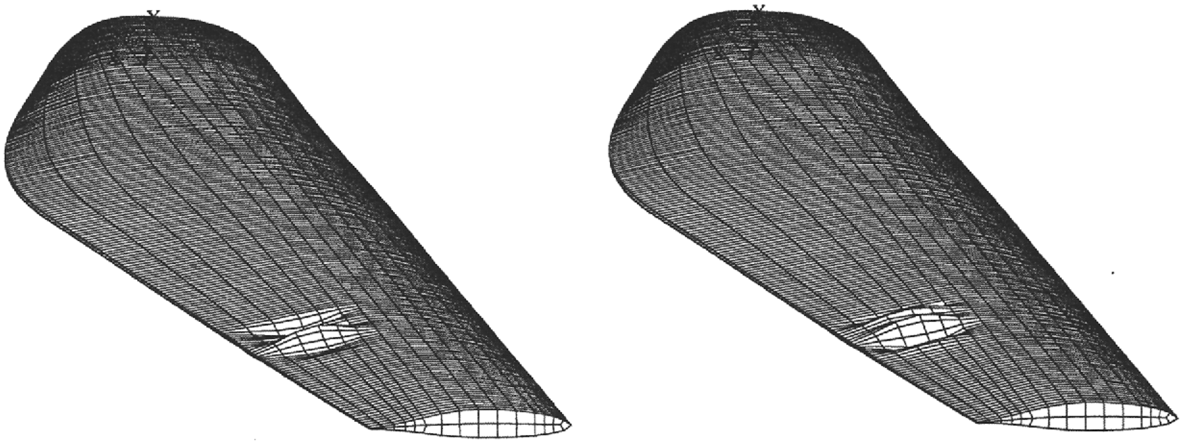

(c) 3rd mode

(d) 4th mode

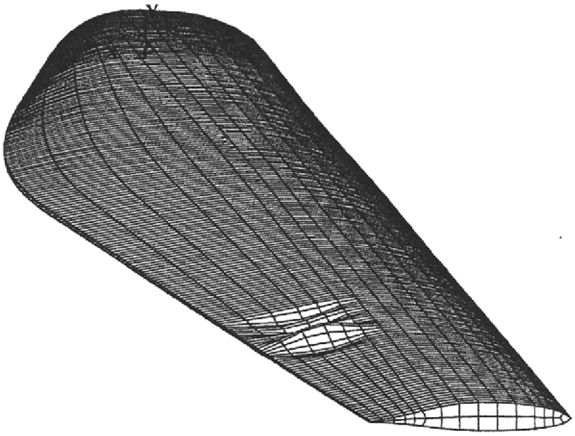

(e) 5th mode

Mode Shape	Load Factor
1st mode (a)	0.49
2nd mode (b)	0.51
3rd mode (c)	0.63
4th mode (d)	0.65
5th mode (e)	0.77
Reference Load	4200 lb

(f) Mode vs. Load Summary

Figure 15: Eigen buckling modes (with trailing edge balsa dropped at $z = 219$ in) for a distributed *reference load* of 4200 lbs (133 MPH wind speed). The *load factor* is the fraction of the reference load likely to induce the given buckling mode. Maximum displacement is scaled to 1 inch.

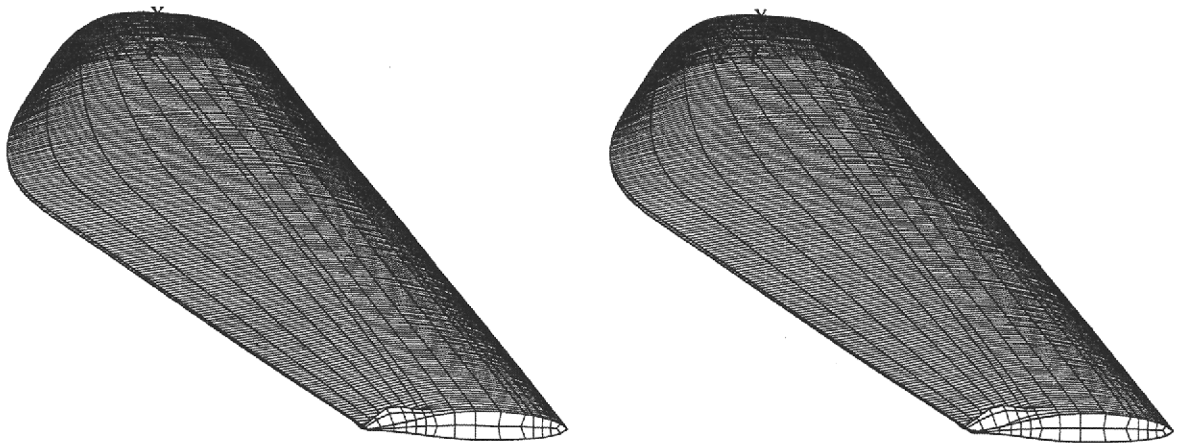

(a) 1st mode (b) 2nd mode

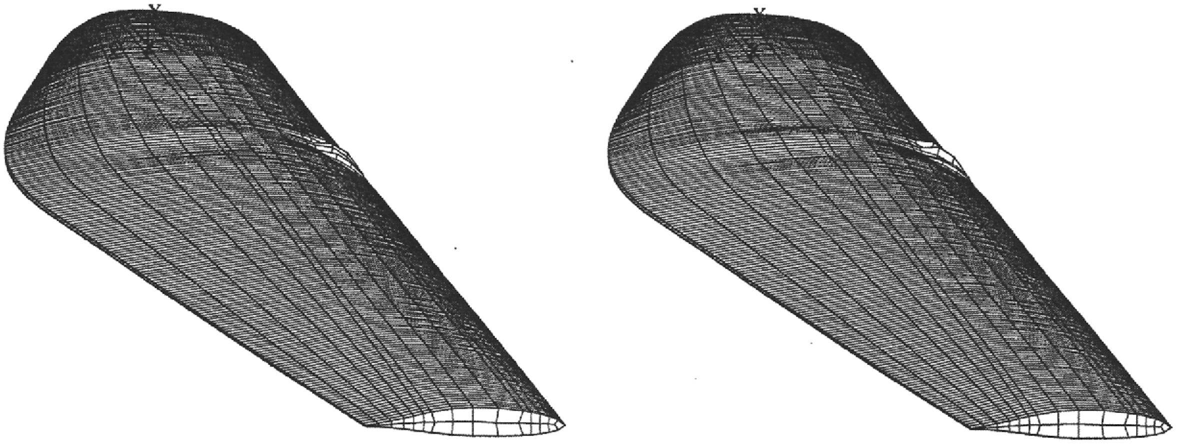

(c) 3rd mode (d) 4th mode

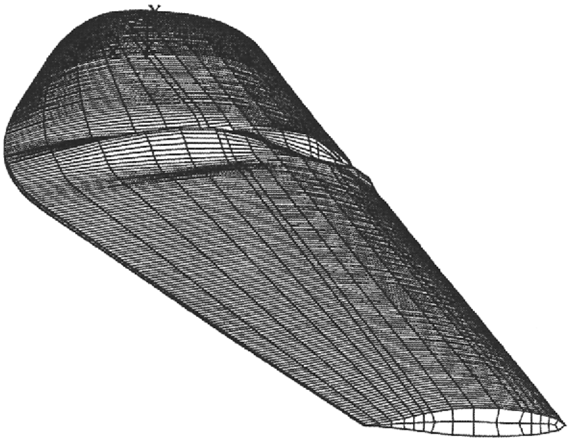

(e) 5th mode

Mode Shape	Load Factor
1st mode (a)	NA
2nd mode (b)	NA
3rd mode (c)	2.7
4th mode (d)	2.7
5th mode (e)	2.7
Reference Load	4200 lb

(f) Mode vs. Load Summary

Figure 16: Eigen buckling with balsa in the spar ([$\pm 45/0_2/\pm 45$/balsa/$\pm 45/0_2/\pm 45$], overall thickness = 0.529 in) for a distributed *reference load* of 4200 lbs. The *load factor* is the fraction of the reference load likely to induce the given buckling mode. Maximum displacement is scaled to 1 inch.

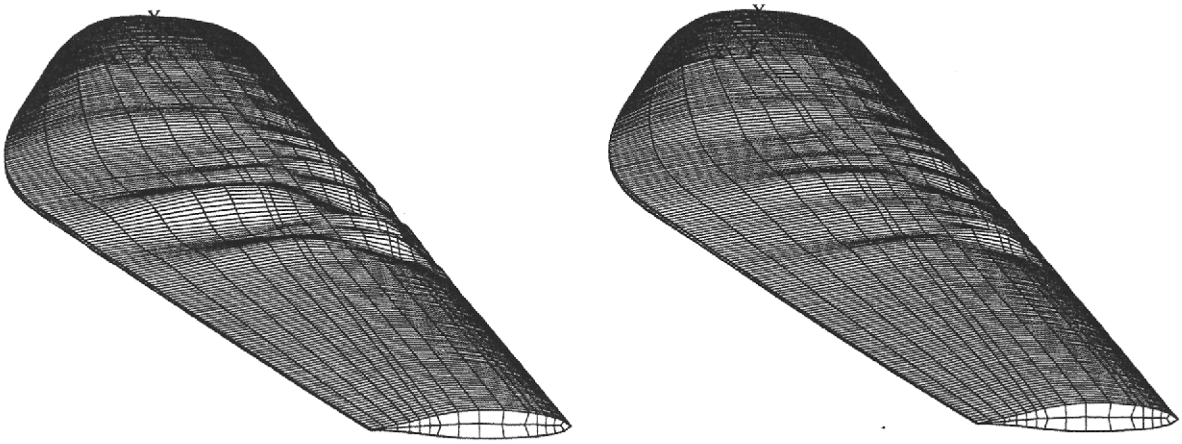

(a) 1st mode

(b) 2nd mode

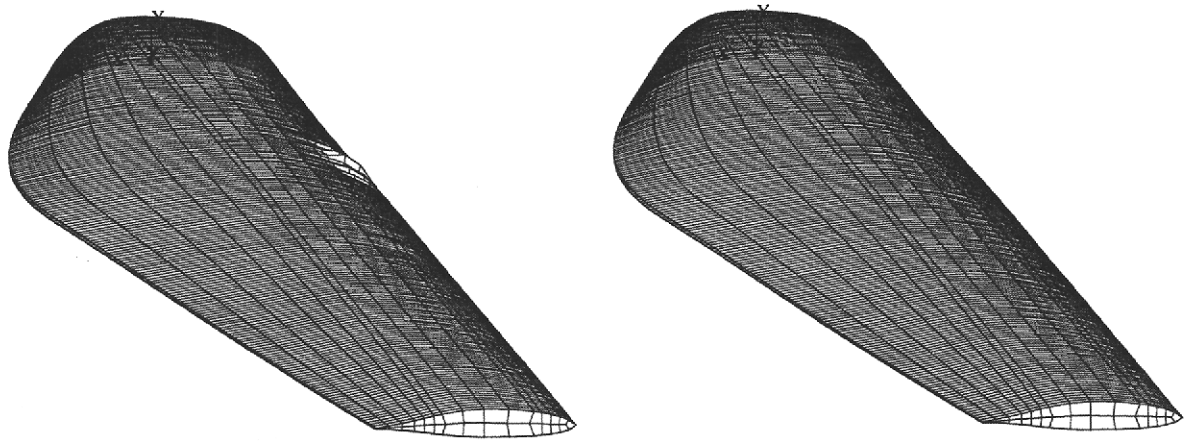

(c) 3rd mode

(d) 4th mode

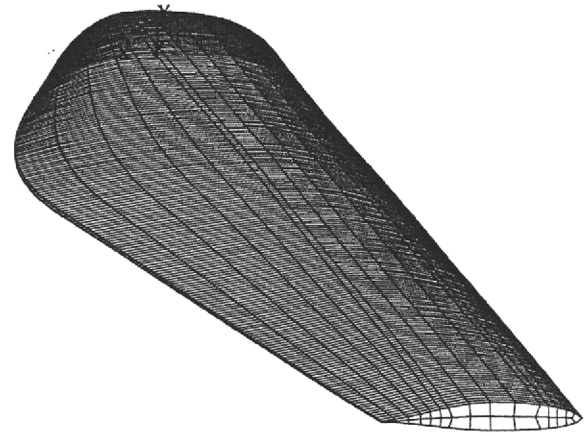

(e) 5th mode

Mode Shape	Load Factor
1st mode (a)	2.85
2nd mode (b)	2.87
3rd mode (c)	2.88
4th mode (d)	2.88
5th mode (e)	2.88
Reference Load	4200 lb

(f) Mode vs. Load Summary

Figure 17: Eigen buckling without balsa in the spar ($[\pm 45/0_2/\pm 45]_s$, thickness ≈ 0.16 in) for a distributed *reference load* of 4200 lbs. The *load factor* represents the fraction of the reference load that is likely to induce the given buckling mode. Maximum displacement is scaled to 1 inch.

Early in the design, the position and layup of the spar were defined in a rather arbitrary fashion. For all of the previous analysis, the spar itself was positioned in the vertical (*xz*) plane, as defined by the coordinate system that was used to position and define the shape of the airfoils throughout the span of the blade (see Figure 2). With the layup schedule reasonably well defined, attention was focused on the position of the spar (shear web).

Because the last iteration of the buckling analyses indicated that buckling was of minimal concern, the spar was positioned using criteria other than buckling. In particular, the chord-wise position of the spar at the tip of the blade was varied while the position of the spar at the root end of the blade was held constant. The spar was then defined to lie along the line connecting these two points in the xy plane. According to Zuteck (1997b), for an operational wind turbine, blade efficiency decreases by ~5% for each one degree change in the angle of attack. Blades that lack torsional stiffness can rotate as much as five degrees under operational loads leading to dramatic drops in output efficiency. For the analyses, both twist and strain were monitored while the spar position was changed. The only parameter that varied in any significant fashion was blade twist, as illustrated in Figure 18.

Again, the load was applied as a bilinear pressure distribution with a peak at 25% of the chord (Figure 11), implying that the center of pressure was at 42% of the chord. As a result, it seemed reasonable that as the position of the spar moved toward the tail, the pressure distribution would generate a larger moment about the blade's shear center, leading to a significant increase in blade twist. However, through further evaluation, it was determined that the variations in blade twist

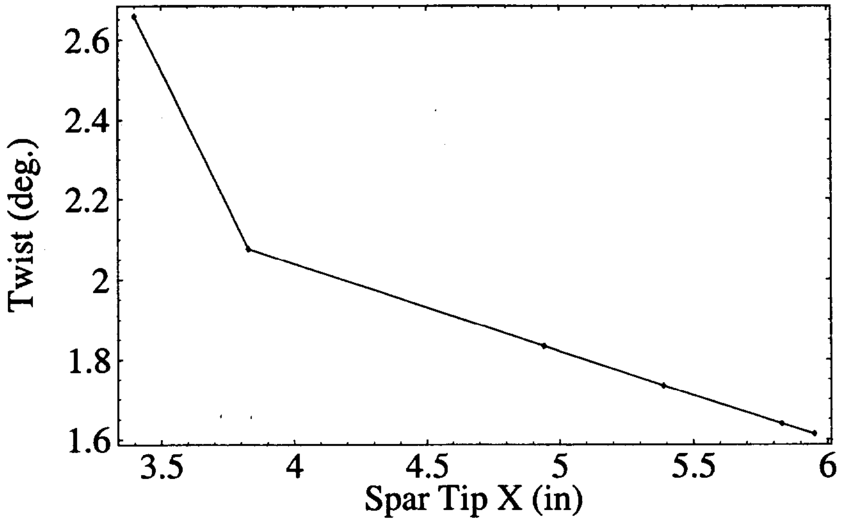

Figure 18: Blade twist at the tip as a function of spar position (*x*) at the blade tip, with the blade under a 4200 lb distributed load. *x* is the distance aft of the one-quarter chord position.

resulted predominantly from variations in the coupling between bending and twisting (sometimes called flat-pitch coupling) as the spar position was varied.

To minimize the coupling without putting the spar in a radical position, the spar was positioned at the tip of the blade at an x coordinate of 4 inches (the coordinate system is displayed in Figure 2). With the spar repositioned in the blade model, the eigen buckling analysis was repeated; the results are shown in Figure 19. In this case, the eigen buckling model indicates that buckling will not take place until a distributed load approaches or exceeds $\sim 9,500$ lbs, 2.28 times the maximum expected wind load. Though this buckling load factor was a significant reduction from the previous load factor of 2.85 ($\sim 12,000$ lbs), which was based on a spar tip positioned at $x = 0$, the overall load required for buckling was still considered conservative.

6.2.3 Non-linear Buckling

Because eigen buckling modeling methods usually yield unconservative estimates for the buckling loads, non-linear buckling models were used to validate and further evaluate the geometric stability of the blade under extreme wind conditions. In particular, the blade was iteratively loaded with an automatic time stepping scheme and a distributed pressure load that was increased in a steady fashion until the load displacement showed a tendency for non-linearity, such that the FE code ANSYS (V54) could no longer determine an equilibrium state. As an example, consider Figure 20.

In Figure 20, the buckled geometry is illustrated in the top half of the figure along with a cross section of the blade near the region that buckled. The lower half of the figure includes a plot of the load factor vs. tip displacement with an inset plot of load factor vs. cumulative iterations. In each of these plots, completed load iterations are indicated by unfilled diamonds.

As mentioned previously, the FE code uses an automatic time (load) stepping scheme as it loads the blade. If deformation continues in a relatively linear fashion, the code can determine the equilibrium configuration for the deformed geometry quite readily based on linear extrapolation from previous load steps. However, if deformation proceeds in an increasingly nonlinear fashion relative to previous load increments, then the FE code must "search" for an equilibrium configuration for the deformed geometry. Often to find an equilibrium configuration, the FE code must decrease the size of the load increment so that a linear extrapolation of the previous deformed configuration serves as a reasonable starting point for the new deformed geometry.

As a consequence, in Figure 20, tightly grouped load increments indicate deformation is tending toward nonlinear behavior. In most cases, such nonlinear tendencies indicate the possible onset of buckling. If the FE code cannot determine a new equilibrium configuration for the next load increment, there is a possibility that the geometry has become unstable and will no longer support added load, or may not support the added load without "snapping through" into a substantially different deformed configuration. As a consequence, when the load increments became small in

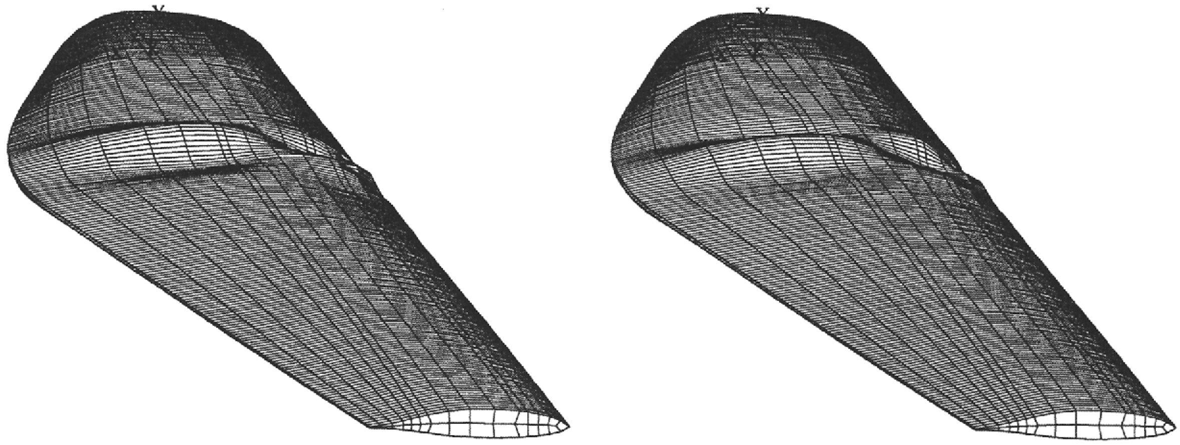

(a) 1st mode

(b) 2nd mode

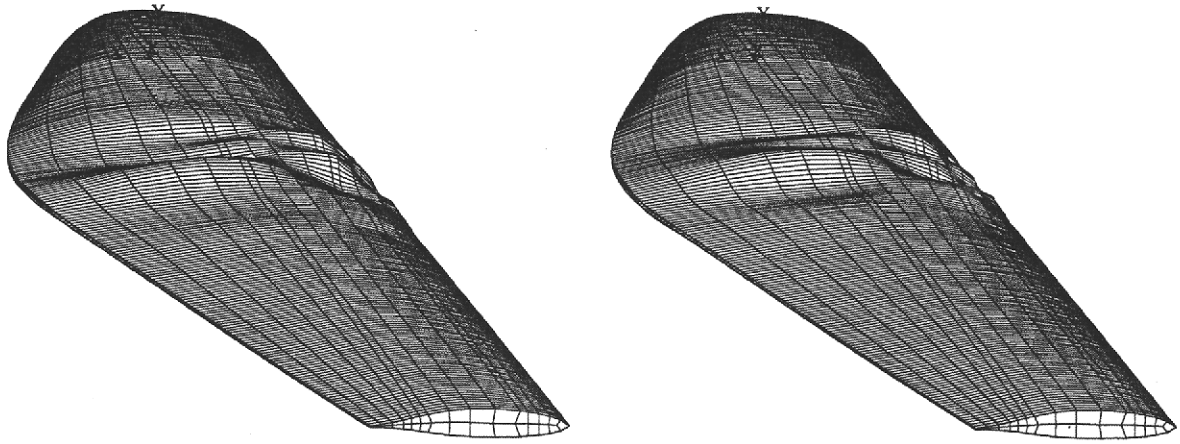

(c) 3rd mode

(d) 4th mode

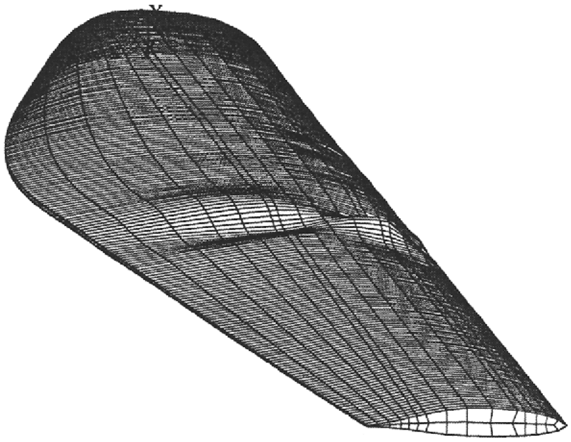

(e) 5th mode

Mode Shape	Load Factor
1st mode (a)	2.28
2nd mode (b)	2.29
3rd mode (c)	2.50
4th mode (d)	2.52
5th mode (e)	2.60
Reference Load	4200 lb

(f) Mode vs. Load Summary

Figure 19: Eigen buckling with the spar tip positioned at $x = 4$. The blade was loaded with a distributed *reference load* of 4200 lbs (133 MPH wind speed). The *load factor* is the fraction of the reference load likely to induce the given buckling mode. Maximum displacement is scaled to 1 inch.

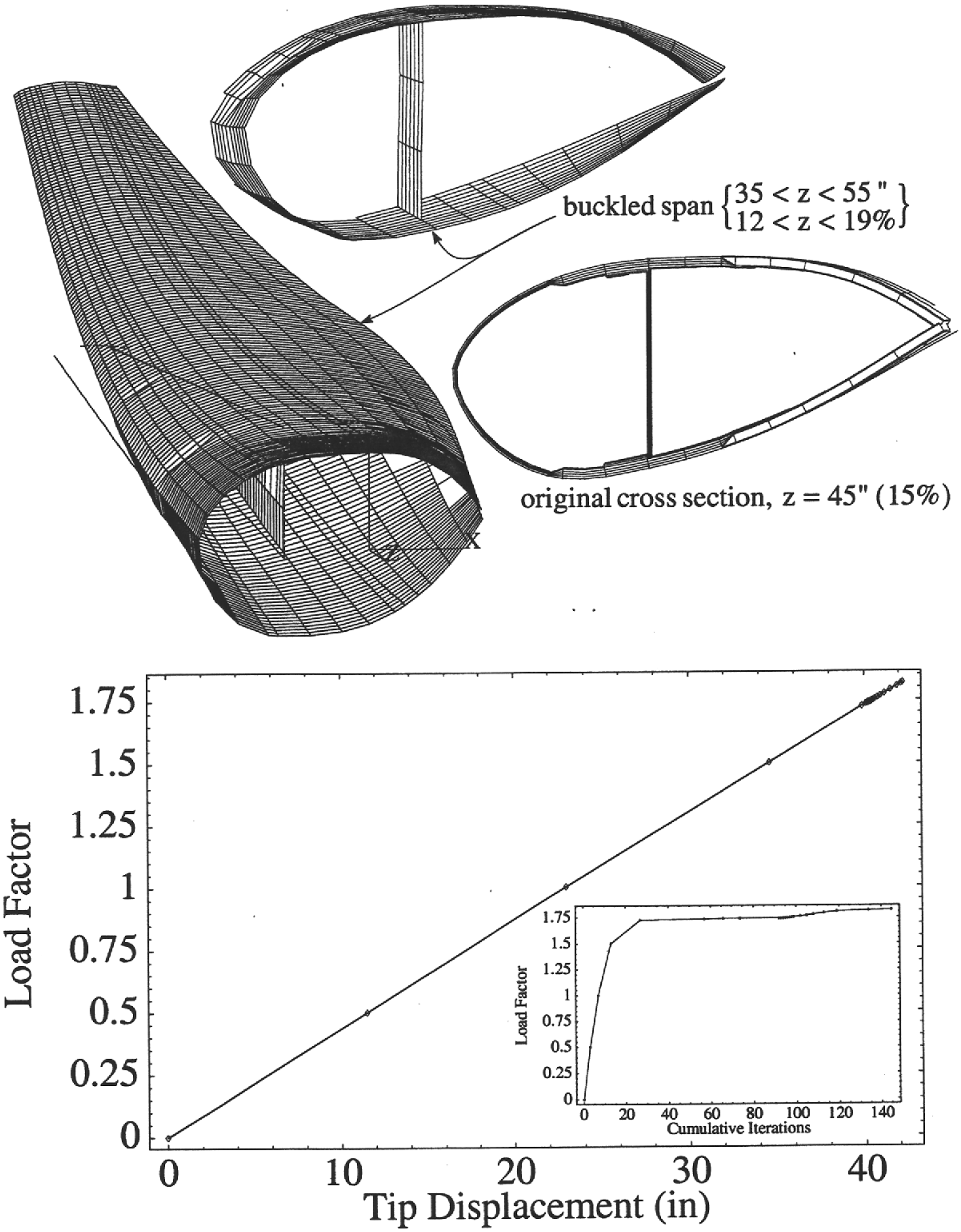

Figure 20: Non-linear buckling with no defects. The blade was loaded with a distributed *reference load* of 4200 lbs, corresponding to an extreme wind speed of 133 MPH. The *load factor* is the fraction of the reference load.

conjunction with the appearance of surface irregularities, as displayed in Figure 20, and the FE code could not converge to an equilibrium configuration, it was assumed that the blade was beginning to buckle. Therefore, the analysis results displayed in Figure 20 indicate that buckling was likely to take place as the load factor approached 1.8 ($\sim$7,500 lbs). Notice that this is substantially less than the load factor of 2.28 estimated by the eigen buckling technique (Figure 19). However, the difference is reasonable based on the history of the two techniques (Bushnell, 1981). In general, nonlinear buckling models are considered more accurate.

With nonlinear buckling models, it was possible to evaluate the effect that defects had on the buckling stability of a structural component. To study the sensitivity of the composite blade to defects, nodes were randomly perturbed or moved from their predefined positions. Deformation was defined normal to the skin of the blade using random numbers derived from a normal distribution that has a standard deviation (σ) of 0.01 inches. For such a distribution, nodes defects (displacements) will in general be less than $\pm$0.03 inches (3σ). A standard deviation of 0.01 inches was chosen only because is provided a reasonable (order of magnitude) approximation of expected defects. The results of three such analyses are presented in Figures 21 through 23. Each analysis used a different set of random defects. As a consequence, each case buckled in a slightly different manner. Notice, however, that in all three cases the model indicates that buckling begins for load factors greater that 1.7 ($\sim$7000 lbs). Strain displacement data was recorded for each of these analyses and is reported in Table 5. Based on these analyses, the modeled blade is expected to be relatively insensitive to defects relative to the load required for buckling.

6.3 Discussion

Of the two sets of extreme loads considered (§6.1 & §6.2), the extreme (133 MPH) wind condition (§6.2) served to place the tightest constraints on the GRP blade design. For this load case, FE results indicated that ultimate strain capacity would be reached when the modeled pressure load was increased by a factor of 1.8 (§6.2.1), while buckling capacity would be reached when the modeled pressure load was increased by a factor of 1.7 or more (§6.2.3). In essence, these analyses indicate that relative to loads considered, the blade was designed with a safety factor of $\sim$1.7.

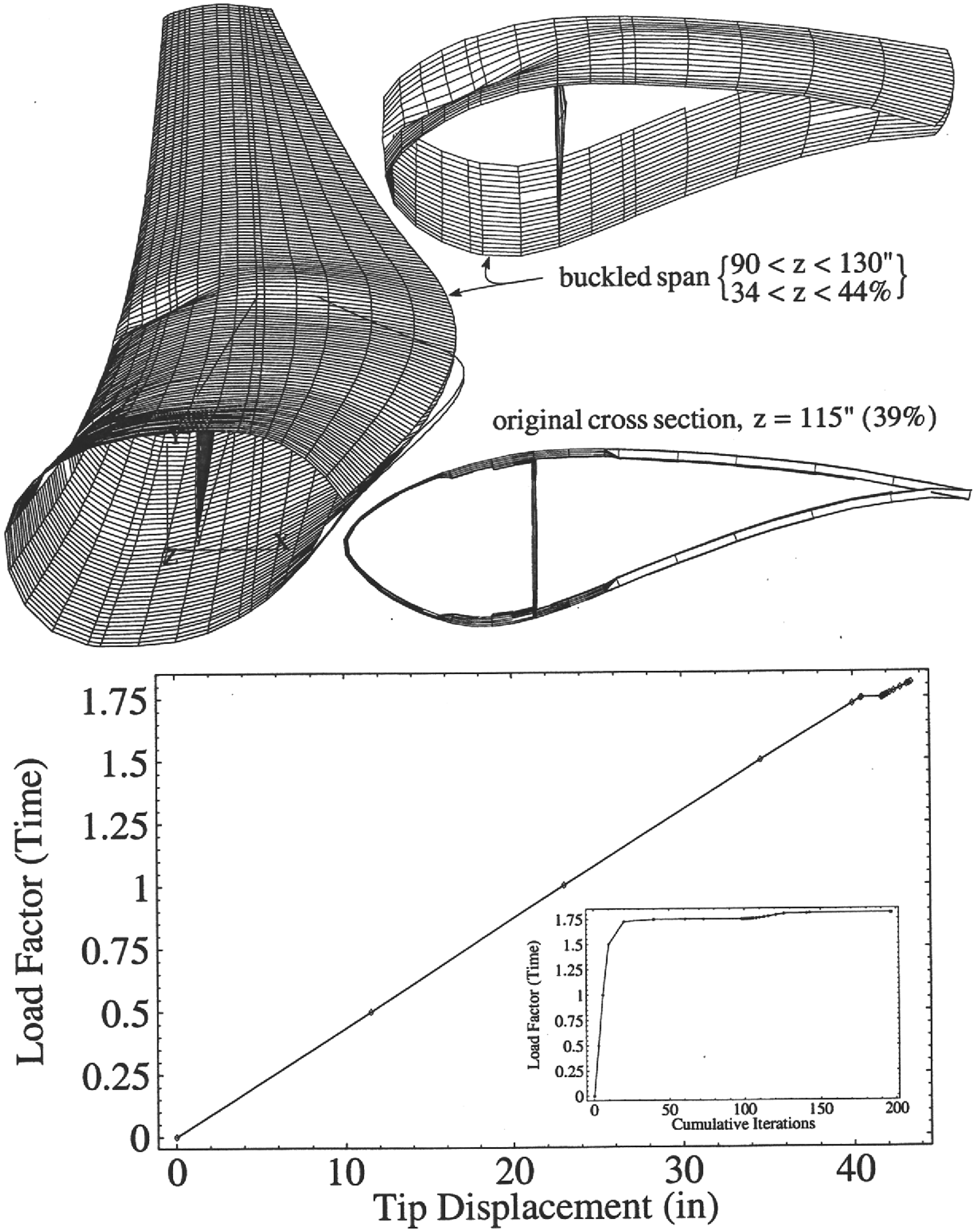

Figure 21: Non-linear buckling with random node defects (X19980625, normal distribution with $\sigma = 0.01$ in) for a distributed *reference load* of 4200 lbs, corresponding to an extreme wind speed of 133 MPH. The *load factor* is the fraction of the reference load.

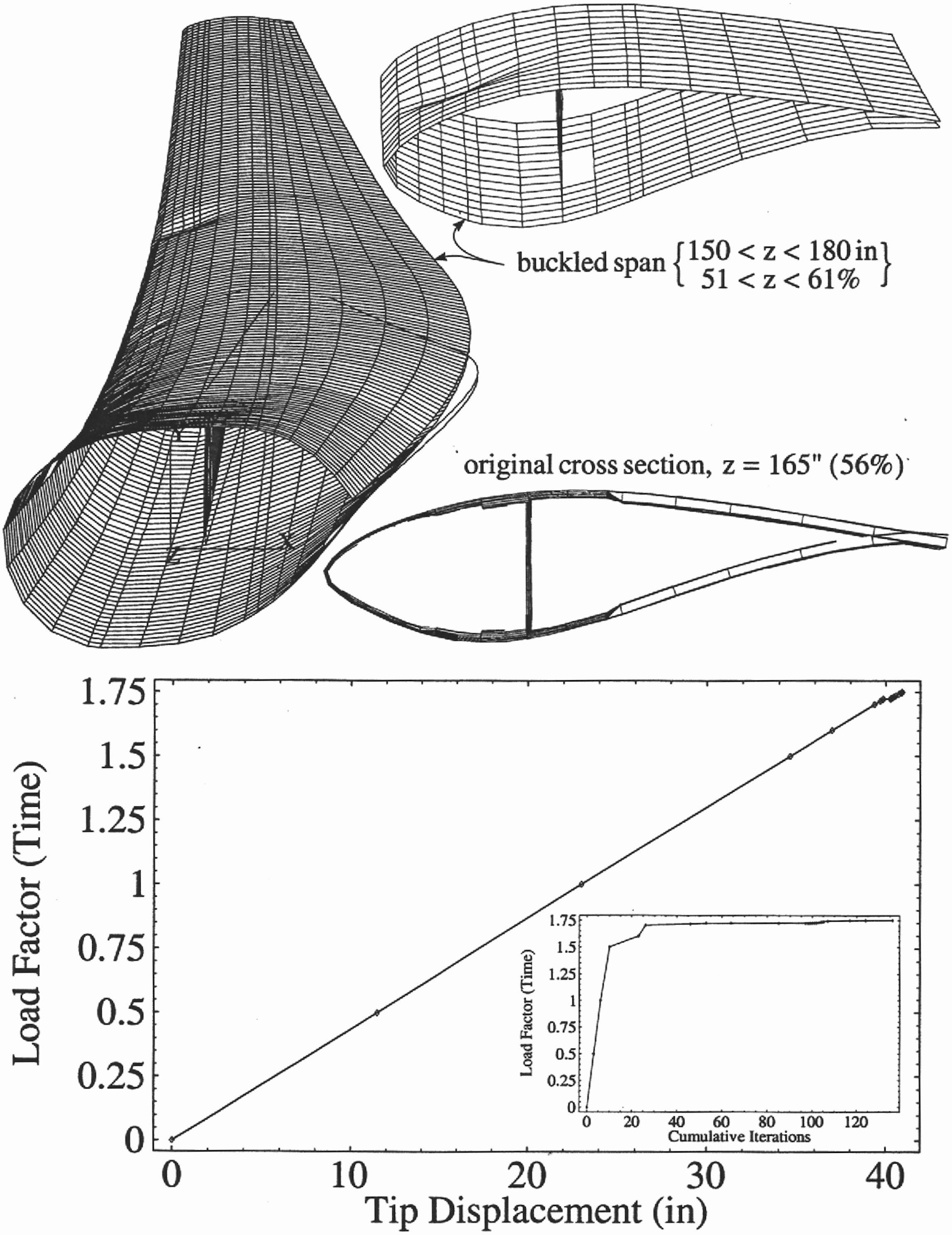

Figure 22: Non-linear buckling with random node defects (X19980627, normal distribution with $\sigma = 0.01$ in) for a distributed *reference load* of 4200 lbs, corresponding to an extreme wind speed of 133 MPH. The *load factor* is the fraction of the reference load.

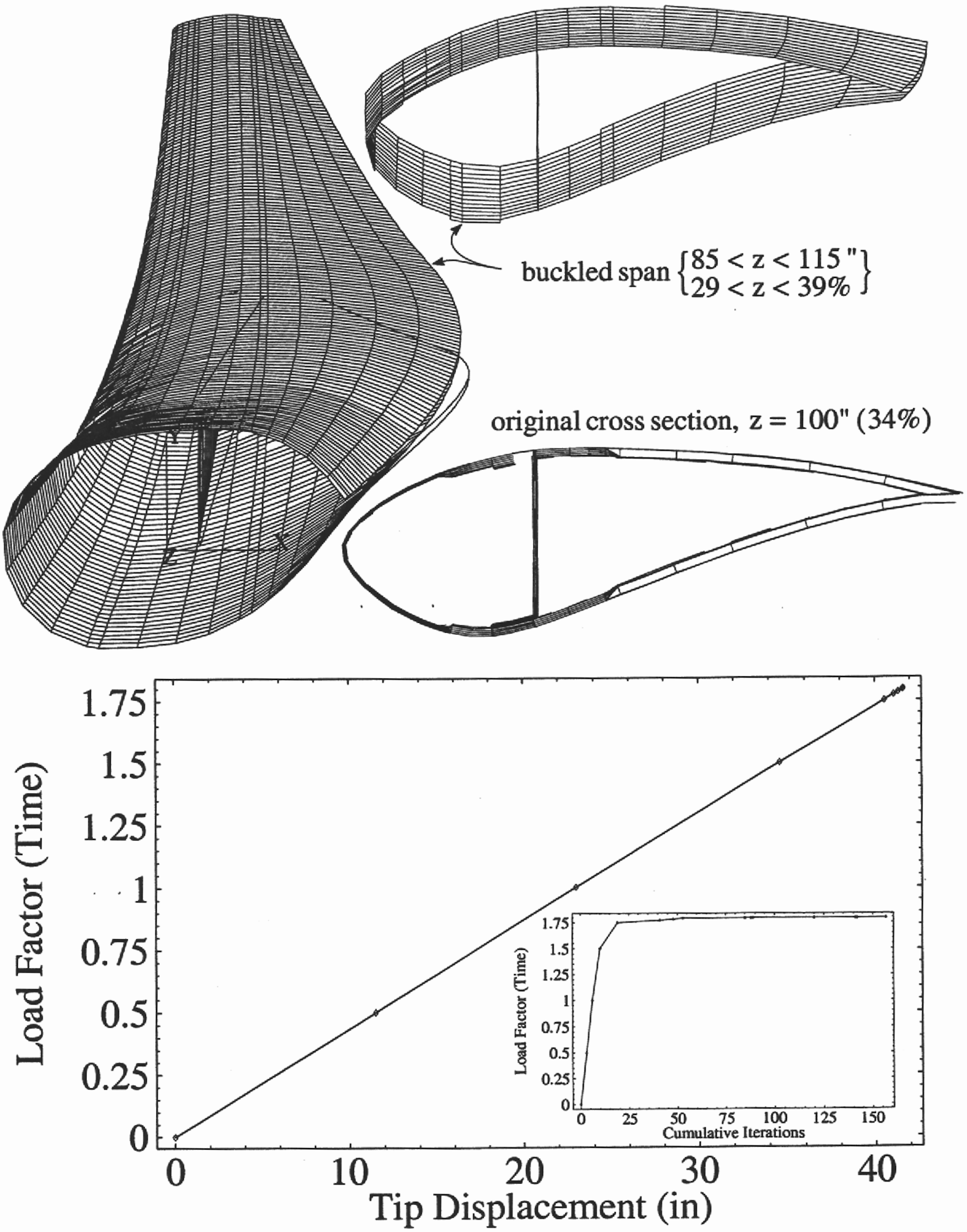

Figure 23: Non-linear buckling with random node defects (X19980630, normal distribution with $\sigma = 0.01$ in) for a distributed *reference load* of 4200 lbs, corresponding to an extreme wind speed of 133 MPH. The *load factor* is the fraction of the reference load.

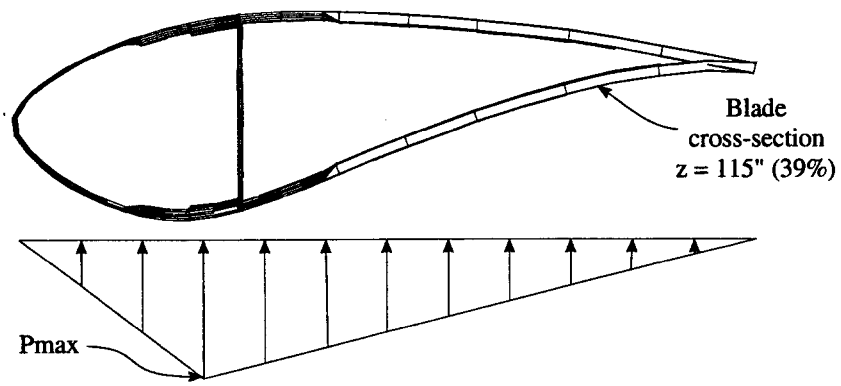

	Pmax@25%	No Defects	X19980625	X19980627	X19980630
Flapwise Force @ Root (lbs)	4202 / 1	7499 / 1.819	Not Available	7202 / 1.75	7381 / 1.795
Flapwise Mom. @ Root (in lbs)	602,000	1,072,000	NA	1,033,000	1,047,000
Max (Tens.) fiber (x) strain {x,y,z} loc	0.41% [4822] {-4.2, -5.2, -43.0}	1.07% [5663] {-6.8, 1.9, -47}	NA	0.66% [3606] {-4.2, -5.5, -43.0}	0.94% [5663] {-6.8, 1.9, -47}
Min (Comp.) fiber (x) strain {x,y,z} loc	-0.43% [7082] {-4.2, 3.4, -43.0}	-1.12% [5655] {-5.5, 2.7, -45}	NA	-0.87% [6895] {-1.9, 2.5, -159}	-1.01% [5655] {-5.5, 2.7, -45}
Max (Tens.) trans (y) strain {x,y,z} loc	0.23% [7467] {-6.9, 1.9, -41.8}	1.39 [5663] {-6.8, 1.9, -47}	NA	1.03% [6279] {-2.5, 2.3, -163}	1.28% [5663] {-6.8, 1.9, -47}
Min (Comp.) trans (y) strain {x,y,z} loc	-0.25% [5657] {-5.9, -4.9, -41.8}	-2.31% [5603] {-4.2, 3.4, -47}	NA	-1.26% [4929] {-6.6, -0.2, -165}	-2.02% [5603] {-4.2, 3.4, -47}
Max (Tens.) thick (z) strain {x,y,z} loc	0.14% [9408] {.43, 4.4, -41.8}	1.28% [5603] {-4.2, 3.4, -47}	NA	0.53% [4929] {-6.6, -0.2, -165}	1.16% [5603] {-4.2, 3.4, -47}
Min (Comp.) thick (z) strain {x,y,z} loc	-0.15% [3080] {.43, -5.2, -41.8}	-1.07% [5663] {-6.8, 1.9, -47}	NA	-0.57% [6279] {-2.5, 2.3, -163}	-0.96% [5663] {-6.8, 1.9, -47}
Min (Comp.) shear (xy) strain {x,y,z} loc	0.35% [7082] {-4.2, 3.4, -43.0}	1.49% [5671] {-7.8, 0.8, -49}	NA	1.32% [7563] {0.2, 2.8, -169}	1.28% [5671] {-7.8, 0.8, -49}
Tip Disp (in)	23.2	42.9	NA	41.5	42.3

Table 5: Comparison of strains, loads, and displacements from nonlinear buckling analyses. The first case (Pmax25%) denotes a linear analysis with a distributed load of 4200 lbs. The other cases refer to the nonlinear analyses indicated by the respective headers (Figures 20 through 23).

7 Summary

A fiberglass blade was designed for the AOC 15/50 wind turbine through the use of finite element (FE) analysis techniques with special consideration given to the minimization of manufacturing complexity and cost. Following the design of a previously designed stiff laminated-wood blade, the FE model indicated that the natural frequencies of the composite blade are all above 3.5 Hz but are likely to vary significantly as a function of the mass associated with the tip brake structure. When compared to a rotational frequency on the order of 1 Hz and a first tower frequency of 1.7 Hz, the primary concern is due to the possibility of a mode interaction between the tower and the blade if the mass associated with the tip brake is sufficient to drive the blade frequency down to approximately 3.4 Hz (twice the fundamental frequency of the tower), making blade-tower resonance a possibility.

The blade design was also designed to withstand extreme wind loads, with wind speeds up to 133 MPH (with the wind turbine in a shutdown mode). For such a load case, the FE model indicated that peak strains occur where blade layup transitions from the heavy root layup to a thinner outboard layup. In the span-wise (primary-fiber) direction, peak compressive strains are approximately -0.41% ($\sim$45% of ultimate); in the circumferential (transverse-fiber) direction, peak tensile strains are $\sim$0.21% ($\sim$54% of ultimate). The FE model with non-linear geometry effects included indicated that buckling is not likely to occur until the statically-equivalent distributed-load of 4200 lb is exceeded by more than 70%.

Yaw effects due to extreme wind shear were also considered. In one case, inertial loads were applied to represent a yaw velocity of 45 deg s^{-1}; in a second case, inertial loads were applied to represent a yaw acceleration of 470 deg s^{-2}. Both of these cases yielded lower strains than those resulting from the statically equivalent wind speed load of 4200 lb.

For this initial design phase, the analyses presented above were deemed sufficient, with the modeled design meeting all load-based criteria. The next phase of the design will focus on the details of the root-hub connections and how the loads can best be transferred from the blade to the hub. Also of interest will be the design of the build-up for the tip brake attachment, while trying to minimize weight. In essence, the overall design has been completed, but many details remain.

References

ANSYS (V5.4). *Engineering Analysis System.* Swanson Analysis Systems, Inc., Houston, Pennsylvania. 4, 36

Blevins, R. D. (1977). *Flow-Induced Vibration.* Van Nostrand Reinhold, New York. 16

Bushnell, D. (1981). Buckling of shells—pitfalls for designers. *AIAA Journal*, 19(9):1183–1226. 39

Fox, R. W. and McDonald, A. T. (1978). *Introduction to Fluid Mechanics.* Wiley, New York. 23

Frost, W. and Aspliden, C. (1994). Characteristics of the wind. In Spera, D. A., editor, *Wind Turbine Technology: Fundamental Concepts of Wind Turbine Engineering*, pages 371–445. American Society of Mechanical Engineers Press, New York. 21

Gere, J. M. and Timoshenko, S. P. (1997). *Mechanics of Materials.* PWS, Boston. 8, 11

Gross, E., Simmermacher, T., and Zadocks, R. I. (1999). Application of damage detection techniques using wind turbine modal data. In *AIAA, Aerospace Sciences Meeting and Exhibit, 37th, Reno, NV, Jan 11-14 1999*, pages 230–235, AIAA Paper 99-0047. American Institute of Aeronautics and Astronautics. 16

Gross, E. G. (1999). Damage detection in a wind turbine blade using modal analysis. Master's thesis, University of Texas, El Paso. 17

Johnson, B. (1996). *AOC 15/50 Blade Loads.* Atlantic Orient Corporation, Norwich, VT USA. Personal Communication (Fax). 16, 17, 22, 23

Lissaman, P. B. (1994). Wind turbine airfoils and rotor wakes. In Spera, D. A., editor, *Wind Turbine Technology: Fundamental Concepts of Wind Turbine Engineering*, pages 283–321. American Society of Mechanical Engineers Press, New York. 3

Liu, H. (1991). *Wind Engineering: A Handbook for Structural Engineers.* Prentice-Hall, Englewood Cliffs, NJ. 23

Mandell, J. F. and Samborsky, D. D. (1997). DOE/MSU composite material fatigue database: Test methods, materials, and analysis. Contractor Report SAND97-3002, Sandia National Laboratories, Albuquerque, NM USA. 6, 6

NREL (1994). Catalog of SERI airfoils designed for horizontal-axis wind turbines. Technical report, National Renewable Energy Laboratory, Golden, CO USA. 3

Popov, E. P. (1990). *Engineering Mechanics of Solids.* Prentice Hall, Englewood Cliffs, New Jersey. 8, 11

Rumsey, M., Hurtado, J., Hansche, B., Simmermacher, T., Carne, T., and Gross, E. (1998). In-field monitoring of wind turbines. *Sound and Vibration*, pages 14–19. 16

Sachs, P. (1978). *Wind Forces in Engineering.* Pergamon Press, Oxford, 2nd edition. 21, 24

Sullivan, T. (1981). A review of resonance response in large, horizontal-axis wind turbines. In Thresher, R., editor, *Proceedings, Wind Turbine Dynamics Workshop*, volume NASA Conference Publication 2185, DOE Publication CONF-810226, pages 237–244, NASA Lewis Research Center, Cleveland, OH. National Aeronautics and Space Administration. 17

Tangler, J. and Somers, D. (1985). Advanced airfoils for HAWTS. In *Proceedings, Wind Power '85 Conference*, volume SERI/CP-217-2902, pages 45–51, Washington, D.C. American Wind Energy Association. 3

Tangler, J. and Somers, D. (1986). A low reynolds number airfoil family for horizontal axis wind turbines. In *Proceedings, International Conference on Aerodynamics at Low Reynolds Numbers, London.* 3

Tangler, J. and Somers, D. (1995). NREL airfoil families for HAWTS. NREL TP-442-7109, National Renewable Energy Laboratory, Golden CO. 1, 3

Thresher, R. W., Mirandy, L. P., Carne, T. G., and Lobitz, D. W. (1994). Structural dynamic behavior of wind turbines. In Spera, D. A., editor, *Wind Turbine Technology: Fundamental Concepts of Wind Turbine Engineering*, pages 507–546. American Society of Mechanical Engineers Press, New York. 19

Zuteck, M. (1996). *Flapwise rigidity of the laminated wood blade for the AOC 15/50 wind turbine.* MDZ Consulting, Houston, TX USA. Personal Communication (Fax). 10

Zuteck, M. (1997a). *Edgewise rigidity of the laminated wood blade for the AOC 15/50 wind turbine.* MDZ Consulting, Houston, TX USA. Personal Communication. 10, 10

Zuteck, M. (1997b). *Efficiency vs. angle of attack for a blade in operation.* MDZ Consulting, Houston, TX USA. Personal Communication. 35